

EXECUTIVE SUMMARY

Deanna Durnford
Department of Civil Engineering
Colorado State University

Heather Hevelone Trantham
Department of Civil Engineering
Colorado State University

Dense Non-Aqueous Phase Liquid (DNAPL) source zone characterization is important for risk assessments, feasibility studies and identification of appropriate remediation technologies at DNAPL-contaminated sites. The extent and configuration of the source zone are also important input to multiphase mass transfer models. When a DNAPL displaces water, the interface between fluids is often unstable due to fluid and porous media properties. Solutions stemming from the continuity equation do not consider the stability of the interface at the pore scale. However, many relevant questions need to be answered by pore scale models. How much lateral spreading of the DNAPL can be expected? How much of the pore space was affected by the DNAPL? How much DNAPL is in contact with the groundwater? The model discussed in this abstract can answer these questions.

The stochastic aggregation model (Trantham and Durnford, 1999) uses a modified DLA algorithm (Witten and Sander, 1983) to model the displacement of water by DNAPLs. Using the model, it is possible to look at the displacement of these fluids under different flow rates, changing porous media properties, and in a gravity field. The front configurations produced under these conditions range from viscous fingers to flat fronts. The model uses macroscopic, dimensionless capillary and bond numbers to circumvent the difficulty of defining parameters on the microscale.

A version of the model is available for use on the www.colostate.edu/Depts/CE/ (click on "what's happening"). Trantham and Durnford (1999) can also be downloaded from this site.

Equation [1] is the non-dimensionalized capillary pressure gradient. This is equivalent to the stability criteria used by Saffman and Taylor (1958) and Chuoke (1959). The equation has been macroscopically non-dimensionalized following Hilfer and Øren (1996):

$$\hat{\nabla} \hat{P}_c = \frac{q_w \mu_w l a}{k_w P_d} - \frac{q_{nw} \mu_{nw} l a}{k_{nw} P_d} + \frac{\Delta \rho g l \sin \alpha}{P_d} \quad [1]$$

The macroscopic flux is given by q , μ is the viscosity, k is the intrinsic permeability, P_d is the displacement pressure, l is a macroscopic length, and a is a scaling factor. Subscripts w and nw refer to the wetting and non-wetting phases, respectively.

The scaling factor is necessary when using a macroscopic equation to describe the pore-scale movement of the interface. The density difference between the non-wetting and wetting phases is given by $\Delta\rho$, and $\sin \alpha$ accounts for any angle of inclination from the horizontal.

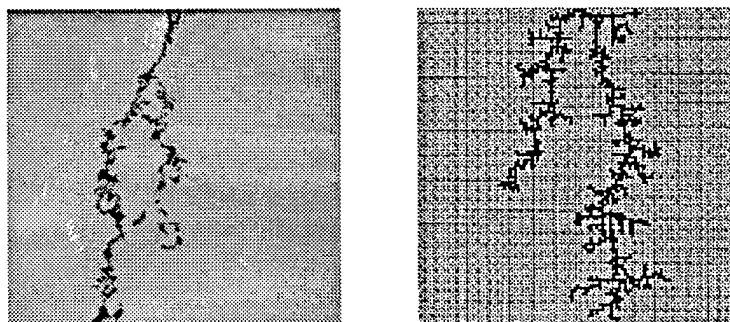
The first two terms in Equation [1] are the macroscopic capillary numbers for the wetting and non-wetting phases, respectively. The last term in Equation [1] is the macroscopic bond number. The linear combination of bond and capillary numbers is called the transition number. The transition number quantifies the stability of the DNAPL-water front as it transitions from viscous fingers to a flat front. The transition number is given as

$$T = (\overline{Ca_w} - \overline{Ca_{nw}}) + \overline{Bo} \quad [2]$$

In the stochastic aggregation model, the sticking probability (Ps), accounts for the changes in front stability. A unique relationship between the sticking probability and the transition number was developed from 43 two-dimensional, DNAPL-water laboratory experiments. The relationship between the sticking probability and the transition number was determined as

$$Ps = 0.1227822|T|^{-1.3240317} \quad [3]$$

The model is validated for homogeneous porous media through comparison with laboratory experiments using Tetrachloroethylene (PERC), 1,2 Dichloroethane (DCA), Carbon Tetrachloride (CTET) and Mobile Pyrogard 53. Examples are shown in Figure 1. The laboratory experiments are shown on the left in Figure 1 with the corresponding model simulation shown on the right. It is important to compare the characteristics of the DNAPL-water displacement, i.e. branching, spreading, and relative thickness of the fingers.



(a)

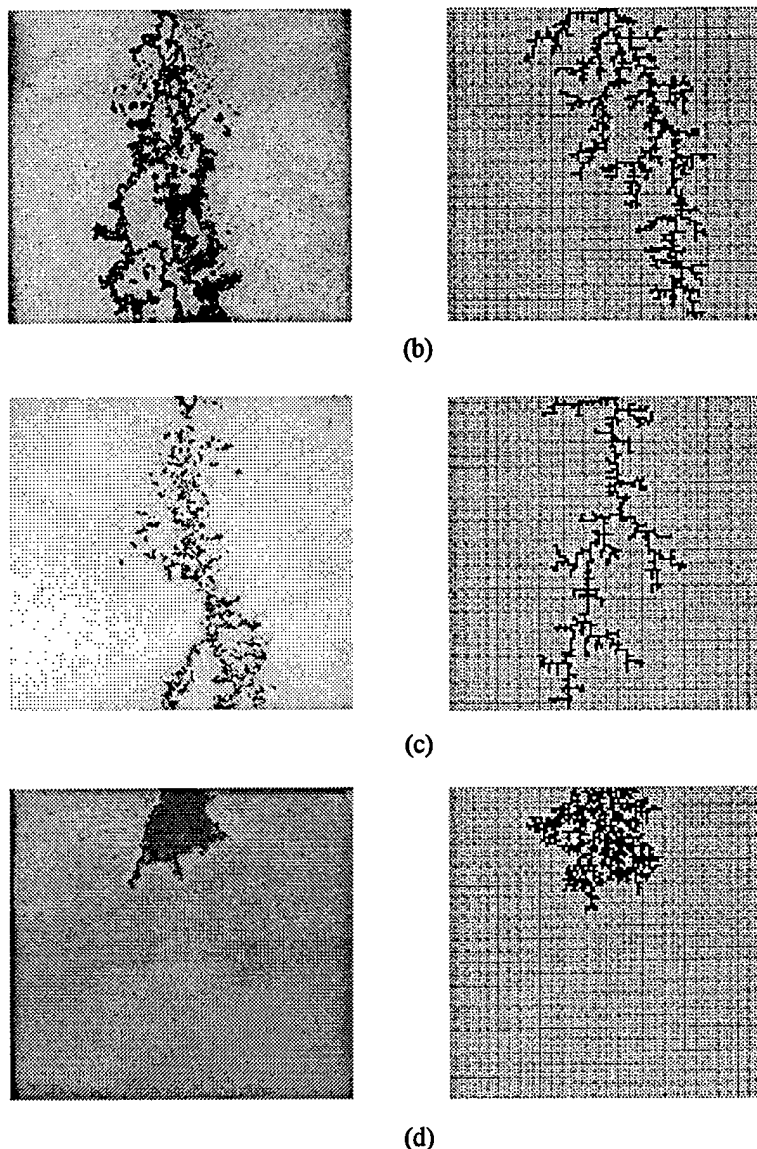


Figure 1. Application of model to DNAPL-water displacement in a two-dimensional flume. (a) PERC 90°, $Q=3 \text{ ml min}^{-1}$, $t=1 \text{ min}$, $T=0.354$, $Ps=0.485$. (b) 1,2 Dichloroethane 45°, $Q=6 \text{ ml min}^{-1}$, $t=1 \text{ min}$, $T=0.473$, $Ps=0.331$. (c) Carbon Tetrachloride 30°, $Q=6 \text{ ml min}^{-1}$, $t=1 \text{ min}$, $T=0.194$, $Ps=1.0$. (d) Mobile Pyrogard 53, 90°, $Q=3 \text{ ml min}^{-1}$, $t=1 \text{ min}$, $T=-2.44$, $Ps=0.037$.

The model is validated for heterogeneous porous media through comparison with the lab experiment of Kueper and Frind (1991). Figure 2 shows the heterogeneous sand packing used by Kueper and Frind (1991). PERC was allowed to infiltrate from the source area at the top of the flume under a constant head of 4 cm. Figure 3 shows the results of Kueper and Frind's (1991) lab experiment on the right with the corresponding model simulation on the left. The model simulations capture the characteristic DNAPL-water displacement and show that the PERC preferentially travels through regions of higher permeability.

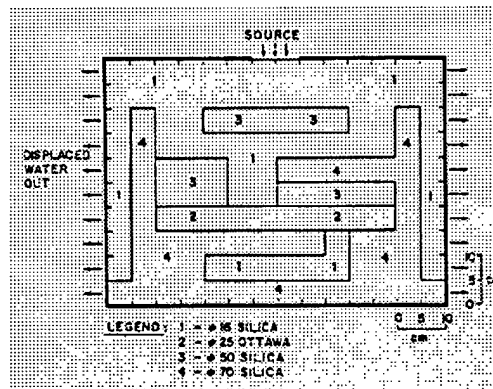


Figure 2. The heterogeneous sand packing of Kueper and Frind's (1991) PERC-water displacement experiment.

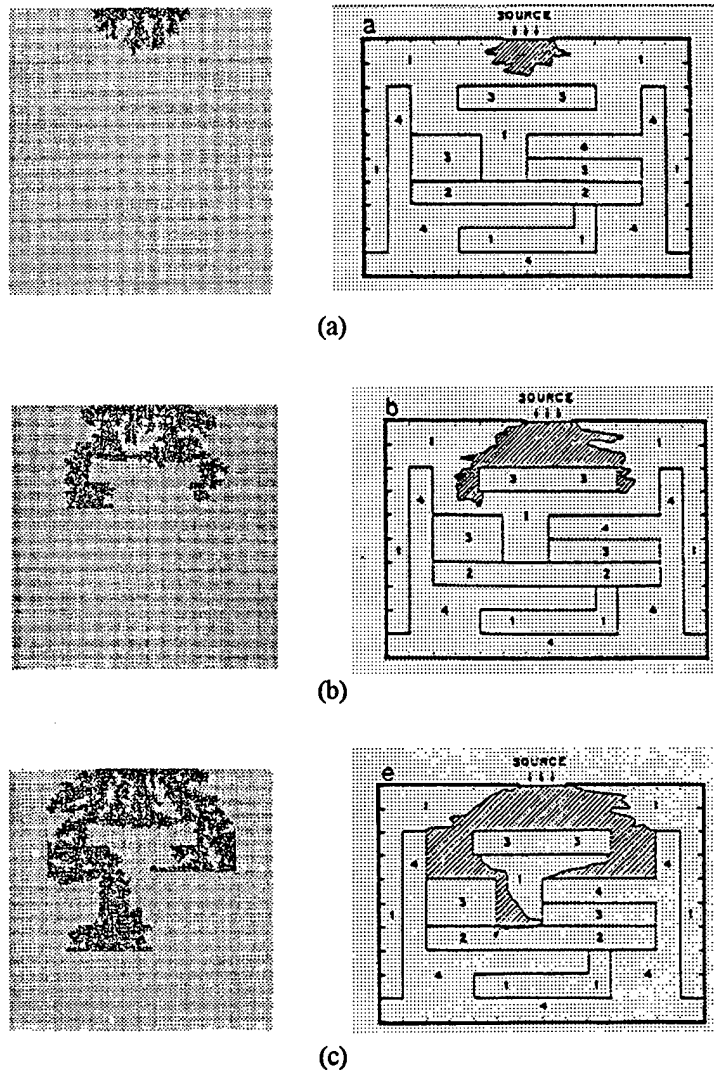


Figure 3. Model simulations (on the left) compared to the experimental results of Kueper and Frind (1991) shown on the right. (a) 34 seconds. (b) 126 seconds. (c) 245 seconds.

The model is applied to the determination of the bulk retention capacity. Bulk retention capacity is a measure of the amount of DNAPL retained per unit volume of aquifer (Johnson and Kueper, 1996). It is used in the determination of DNAPL depth. Changes in bulk retention capacity are investigated with changing inflow rate, intrinsic permeability, and DNAPL viscosity.

The model is currently well formulated for simulating two-dimensional DNAPL-water displacement for a variety of DNAPLs under the conditions of different inflow rates, different angles of inclination from the horizontal, and varying heterogeneous media properties. The comparison of model simulations to laboratory experiments remains limited to visual inspection, as is the case for other models currently attempting to model DNAPL-water displacements. We are currently working on expanding the model to three dimensions and exploring better means of graphical representation of the model's output.

The dissertation submitted by Heather Trantham-Hevelone to Colorado State University is attached as an appendix to this report, without appendices. These are available from the author by request.

Acknowledgments and Disclaimer

This work was sponsored by the Air Force Office of Sponsored Research, USAF, under grant/contract number F49620-95-1-0413 (ASSERT95), parent contract F49620-94-1-0193. The views and conclusions contained herein are those of the authors and do not necessarily represent the official policies, either expressed or implied, of the Air Force Office of Scientific Research or the U.S. Government. The authors gratefully acknowledge the support of the AFOSR and their program managers.

References

- Chuoque, R. L., Van Meurs, P., and van der Poel, C. The instability of slow immiscible, viscous liquid-liquid displacements in porous media, 1959, *Trans. A.I.M.E.*, 216: 188-194.
- Hilfer, R. and Øren, P. E. Dimensional analysis of pore scale and field scale immiscible displacement, 1996, *Transp. Porous Media*, 22: 53-72.
- Johnson, R. L. and Kueper, B. H., Experimental studies of the movement of chlorinated solvent compounds and other DNAPLs in the vadose, capillary and groundwater zones, in *Dense Chlorinated Solvents and other DNAPLs in Groundwater*, ed. J. F. Pankow and J. A. Cherry, 1996, Waterloo Press, Portland, OR, pp. 145-178.

Kueper, B. H. and Frind, E. O. Two-phase flow in heterogeneous porous media 1. Model development, 1991, *Water Resour. Res.*, 27(6): 1049-1057.

Saffman, P. G. and Taylor, G. I. The penetration of a fluid into a porous medium or Hele-Shaw cell containing a more viscous liquid. *Proc. Soc. London, Ser. A*, 1958, 245: 312-331.

Trantham, H. and Durnford, D. S. Stochastic aggregation model (SAM) for DNAPL-water displacement in porous media. Accepted for publication, *J. Contam. Hyd.*, 1999.

Witten, T. A. and Sander, L. M., 1983. Diffusion-limited aggregation. *Physical Review B*, 27(9): 5686-5697.

Appendix

Stochastic Aggregation Model for DNAPL-Water Displacement in Homogeneous and Heterogeneous Porous Media

by

**Heather Hevelone Trantham
Department of Civil Engineering
Colorado State University
Fort Collins, CO**

TABLE OF CONTENTS

1.	Introduction	1
2.	Background	5
2.1	Fluid-Fluid Displacement	5
2.2	Stochastic Modeling Techniques	6
3.	Model Formulation and Calibration	11
3.1	Model Formulation	11
3.1.1	Analysis of Front Stability	11
3.1.2	Stochastic Aggregation Algorithm	17
3.2	Model Calibration	18
4.	Model Confirmation and Scaling in Homogeneous Porous Media	25
4.1	Model Confirmation	26
4.2	Model Scaling.	39
5.	Model Confirmation for Heterogeneous Porous Media	44
5.1	Heterogeneous Model Confirmation	44
5.2	Single Fine/Coarse Lens	44
5.3	Heterogeneous Sand Packing	52
6.	Model Determination of Bulk Retention Capacity	62
6.1	Retention Capacity Determination	63
6.2	Changes in Bulk Retention Capacity with Varying Parameters	66
7.	Model Evaluation	71
7.1	Benefits of the Stochastic Aggregation Model	71
7.2	Limitations of the Stochastic Aggregation Model	73
8.	Summary, Conclusions, and Recommendations	77

References	80
Appendix A: Review of Percolation and Diffusion Limited Aggregation Modeling	88
Appendix B: Model Calibration Parameters and Pictures	99
Appendix C: Model Validation Parameters and Pictures	109

LIST OF TABLES

Table 4.1	Model confirmation cases	23
Table 4.2	Area ratio for a 113 x 113 sub-grid on increasing grid sizes for a sticking probability of 0.01	42
Table 5.1	Sand characteristics and model parameters for the experiments of Illangasekare et al. (1995)	45
Table 5.2	Model Scaling Characteristics	47
Table 5.3	Number of Particles for model simulation of Kueper et al. (1989)	54
Table 5.4	Sand characteristics and model parameters for simulation #1 of Kueper et al. (1989) experiment	54
Table 5.5	Sand characteristics and model parameters for simulation #2 of Kueper et al. (1989) experiment	59
Table 6.1	Model calculated retention capacity values for $Q=59 \text{ ml min}^{-1}$.	64
Table 6.2	Model calculated retention capacity values for $Q=30 \text{ cm}^3 \text{ min}^{-1}$.	65
Table 6.3	Model calculated retention capacity values for $Q=15 \text{ cm}^3 \text{ min}^{-1}$.	65
Table B-1	Model calibration parameters for 1,2 Dichloroethane (DCA)	99
Table B-2	Model calibration parameters for Carbon Tetrachloride (CTET)	99
Table B-3	Model calibration parameters for Tetrachloroethane (PERC)	100
Table B-4	Model calibration parameters for Mobile Pyrogard 53 .	100
Table C-1	Model confirmation parameters for 1,2 Dichloroethane (DCA).	109
Table C-2	Model confirmation parameters for Carbon Tetrachloride (CTET)	109
Table C-3	Model confirmation parameters for Tetrachloroethane (PERC).	110
Table C-4	Model confirmation parameters for Mobile Pyrogard 53 .	110

LIST OF FIGURES

Figure 2.1	The stochastic modeling techniques corresponding to the regimes for which their use is suggested is shown with varying microscopic capillary number and mobility ratio. Adapted from Lenormand's (1987) phase diagram for immiscible fluid-fluid displacement in the absence of gravity.	9
Figure 3.1	Microscopic interface perturbation (adapted from Kueper and Frind, 1988).	12
Figure 3.2	Aggregates formed by stochastic aggregation model simulations with different sticking probabilities. The sticking probability for 3.2(a) and 3.2(b) is 67% and 2%, respectively.	18
Figure 3.3	Relationship between the sticking probability and the area ratio, modeled as a power law function.	21
Figure 3.4	Relationship between the transition number and the sticking probability as a power law function.	23
Figure 4.1	A comparison of the area ratios as calculated from the lab experiments and the model simulations.	29
Figure 4.2	Lab experiments and model simulations for 1,2 Dichloroethane (DCA).	34
Figure 4.3	Lab experiments and model simulations for Carbon Tetrachloride (CTET).	35
Figure 4.4	Lab experiments and model simulations for Tetrachloroethylene (PERC).	36
Figure 4.5	Lab experiments and model simulations for Mobile Pyrogard 53 at different times.	37
Figure 4.6	Lab experiments and model simulations for Mobile Pyrogard 53.	38
Figure 4.7	The decrease in area ratio with increasing grid size shown for a sticking probability of 0.1.	40
Figure 4.8	Model simulations for a sticking probability of 0.1. Figure 4.8(a) shows a model simulation on a 200 x 200 grid. Figure 4.8(b) shows a model simulation on a 600 x 600 grid.	41

Figure 4.9	The area ratio for a 113 x 113 portion of the simulated grid compared for varying grid sizes up to 1000 x 1000.	43
Figure 5.1	The experimental configuration used by Illangasekare, et al. (1995).	45
Figure 5.2	Model simulation of layered system: #30-#70-#30.	48
Figure 5.3	Model simulation of layered system: #30-#16-#30.	50
Figure 5.4	The experimental configuration for Kueper et al. (1989)	52
Figure 5.5	Model simulations compared to the experimental results of Kueper et al. (1989).	55
Figure 5.6	Two model simulations run to match the experiment at 184 seconds show characteristically the DNAPL migration path.	56
Figure 5.7	Second set of model simulations compared to the experimental results of Kueper et al. (1989).	60
Figure 6.1	The bulk retention capacity increases as the flow rate increases for 6 common DNAPLs.	66
Figure 6.2	The bulk retention capacity decreases as the intrinsic permeability increases for 6 common DNAPLs.	67
Figure 6.3	The bulk retention capacity approaches 29 L m ⁻³ with increasing viscosity difference relative to water.	68
Figure 6.4	The portion of Figure 6.3 with viscosity differences ranging between 0 and 2.	69
Figure 6.5	A DNAPL occupying 61% of the pore space.	70
Figure A-1	An aggregate produced by invasion percolation with trapping (Meakin, 1991).	90
Figure A-2	An aggregate produced by Witten and Sander's (1983) original diffusion limited aggregation algorithm.	92
Figure A-3	A DLA simulation from a line seed.	93
Figures B-1 through B-43	Experiments used for model calibration.	101
Figures C-1 through C-33	Experiments used for model validation.	111

CHAPTER 1

INTRODUCTION

Groundwater contamination by non-aqueous phase liquids (NAPLs) has received increasing attention in the last decade. Light Non-Aqueous Phase Liquids (LNAPLs) are liquids with specific gravities less than water. They are associated with the production, refining, and distribution of petroleum products (Bedient, 1994). Dense Non-Aqueous Phase Liquids (DNAPLs) are liquids with specific gravities greater than water. Many commonly used DNAPLs are chlorinated solvents, but there are several that are halogenated organics, PCB mixtures, and pesticides. Typical uses for DNAPLs include metal cleaning and degreasing, dry cleaning, paint removal, and use as adhesives and aerosols (Pankow et al., 1996). DNAPL solubilities in air and water are high enough to far exceed regulatory standards when dissolution occurs in the groundwater even though they are essentially immiscible in water (Mabey et al., 1982). Both lighter and denser NAPLs can contaminate water supply systems, but due to unfavorable viscosity and density differences with water, DNAPLs can penetrate the water table and migrate downward. As vertical migration occurs, a trail of trapped residual is left behind. If lower permeability soils are encountered, small pools of DNAPL may form. Both scenarios can lead to long term contamination.

DNAPL source zone characterization is important for risk assessments, feasibility studies and identification of appropriate remediation technologies at DNAPL-

contaminated sites. The extent and configuration of the source zone are also important input to multiphase mass transfer models. Field and laboratory experiments to determine source zones are either not feasible or not permitted due to the hazardous nature of DNAPLs. Numerical modeling of DNAPL migration provides a solution to this problem, however accurate qualitative and quantitative descriptions of DNAPL source zones are unattainable with commonly used modeling techniques.

In this study, the problem of accurate source zone characterization is looked at in terms of the DNAPL-water interface stability on the pore scale. The objectives of this study are:

- to develop a modeling technique for simulating DNAPL-water displacements at the pore scale.
- to evaluate the modeling technique through comparisons with DNAPL-water displacement studies in homogeneous porous media.
- to apply the new modeling technique to DNAPL-water displacements in heterogeneous media.
- to investigate the use of the modeling technique in calculating bulk retention capacities.

Continuum models are used to simulate the immiscible transport of NAPLs through water-saturated media. However, there is no longer any question that small scale heterogeneities control the movement of DNAPL through soil (Schwille, 1988; Kueper and Frind, 1991a and b; Kueper and Gerhand, 1995, Illangakesare et al., 1995; Held and Illangasekare, 1995a and b; and Illangasekare et al., 1996). While these heterogeneities can be characterized statistically, the commonly available models are ill equipped to

accommodate their influence on multiphase transport (Mercer et al., 1996). Using continuum models to determine fluid-fluid displacements at the pore scale is computationally prohibitive and beyond the capability of available numerical simulators (Poulsen and Kueper, 1992). Invasion percolation (IP) models are used for pore scale fluid-fluid displacement (Chatzis and Dullien, 1985; Li et al., 1986; Wardlaw et al., 1987; Constantinides and Payatakes, 1989; Jerauld and Salter, 1990; Tsakiroglou and Payatakes, 1990; Ferrand and Celia, 1992; Soll and Celia, 1993; Lowry and Miller, 1995; Glass et al., 1995). These are applicable only for capillary-dominated, stable flow. IP models neglect important processes because gravity and viscous forces, in addition to capillary forces govern the flow patterns of many DNAPLs of interest in contaminant hydrology (Schwille, 1988).

DNAPL-water displacements are typically unstable depending on the fluid properties of the DNAPL relative to water. Witten and Sander's (1983) diffusion limited aggregation (DLA) technique has been used to model such unstable processes as dielectric breakdown (Niemeyer et al., 1984; Wiesmann and Zeller, 1986), diffusion-controlled polymerization (Kaufman et al., 1986), chemical dissolution processes (Daccord et al., 1986), solute leaching (Flury and Fluhler, 1995), viscous fingering (Maloy et al., 1985; Chen and Wilkinson, 1985), fluid-fluid displacement in Hele Shaw cells (Kadanoff, 1985; Liang, 1986); and fluid-fluid flow in porous media in the absence of gravity (Paterson, 1984; Lenormand, 1987; Lenormand et al., 1988; Kiriakidis et al., 1991; Fernandez et al., 1991).

The stochastic aggregation modeling algorithm, developed in this study, is based on Witten and Sander's (1983) diffusion limited aggregation (DLA) technique. The

model inputs are the essential properties governing front stability: DNAPL-water viscosity difference, DNAPL-water density difference, intrinsic permeability of the porous media, flow rate, and the inclination angle of the porous media from the horizontal if the domain is two-dimensional. The front stability is evaluated using criteria similar to the instability criteria of Saffman and Taylor (1958) and Chuoke et al. (1959). The background information pertaining to fluid-fluid displacements and stochastic modeling techniques is provided in Chapter 2. The development of the modeling technique is presented in Chapter 3. In Chapter 4, the model is evaluated by comparing model simulations to two-dimensional DNAPL-water displacements in porous media. In Chapter 5, the model is used to simulate three heterogeneous laboratory experiments. An application of the model to the evaluation of bulk retention capacities is examined in Chapter 6, and the benefits and limitations of the modeling technique are discussed in Chapter 7.

CHAPTER 2

BACKGROUND

2.1 Fluid-Fluid Displacement

Depending on the relative fluid properties, immiscible fluid displacements may exhibit unstable flow. An inherently unstable flow regime results when water is displaced by a DNAPL with a lower relative viscosity. Many DNAPLs, including chlorinated solvents, are both more dense and less viscous than water. The term fingering is used as a visual description of these displacements in porous media (Chuoque et al., 1959), but does not necessarily imply unstable flow. Unstable fluid-fluid displacements result in fingered fronts when a small perturbation is caused by a microscopic heterogeneity in a macroscopically homogeneous media (Kueper and Frind, 1988). The velocity of the displacing fluid can contribute to unstable flow regimes (Hill, 1952) in addition to the relative fluid properties. Chuoque et al. (1959) determined the critical wavelength (tip to tip separation between the fingers) as a constraint accounting for the stabilizing or destabilizing influence of the surface tension. The problem is compounded at the pore-scale if such details as wetting films, changing contact angles, and heat and mass transfer are included in the problem description.

The description of fingering in homogeneous porous media depends on the length scale chosen, even when small-scale heterogeneities and gravity are neglected (Homsy, 1987). Chuoque et al. (1959) showed variations in fingering length scales with both

increasing velocity and viscosity difference in homogeneous porous media. Applicability of macroscopic scales decreases with increasing velocity, increasing mobility, or decreasing surface tension (Homsy, 1987). Wetting properties of the two fluids are also important. If the invading fluid wets the medium, then the fingering can be characterized on a macroscopic continuum scale. If the invading fluid is non-wetting with respect to the medium, fingering is confined to the pore scale (Homsy, 1987).

There is no preferred method of numerically modeling immiscible instabilities (Kueper and Frind, 1988). Analytical solutions require many simplifying assumptions due to the nonlinearity of the problem and do not explicitly consider the stability of the interface between the fluids. Other modeling techniques including stochastic aggregation models are equipped to model the effects of pore-scale instabilities by basing the movement on decisions made at the pore scale.

2.2 Stochastic Modeling Techniques

The displacement of one fluid by another in porous media can be represented by particle aggregation where the growing aggregate represents the invading fluid and the space surrounding the aggregate represents the defending fluid. Aggregate growth by irreversible particle collection is a common phenomenon in nature (Sander, 1984), and several modeling techniques can be used for particle aggregation. These include Invasion Percolation (IP) modeling (Wilkinson and Willemsen, 1983), Eden modeling (Sander 1984), ballistic aggregation (Sander, 1984), and DLA (Witten and Sander, 1983). IP modeling is applicable to immiscible fluid displacements dominated by capillary forces (Chatzis and Dullien, 1985; Li et al., 1986; Wardlaw et al., 1987; Constantinides and

Payatakes, 1989; Jerauld and Salter, 1990; Tsakiroglou and Payatakes, 1990; Ferrand and Celia, 1992; Soll and Celia, 1993; Lowry and Miller, 1995). Whereas, IP models simulate stable migration patterns, many DNAPLs move in inherently unstable flow regimes (Schwille, 1988). Other aggregate modeling options are needed to model fluid-fluid displacements where any combination of viscous, capillary, or gravity forces govern the stability of the interface. Neither Eden modeling nor ballistic aggregation describe the growth instabilities characteristic of many processes including fluid-fluid displacement with unfavorable mobility ratios (Sander, 1986). DLA models, however, produce aggregates resulting from unstable phenomenon using a stochastic process. Following Witten and Sander (1983), numerous other researchers have expanded on both the modeling technique and the applications for the model (Meakin and Deutch, 1986; Meakin, 1986; and Jullien et al., 1984). Meakin (1988) provides a thorough review of DLA as a model for kinetic growth phenomena. A review of IP and DLA modeling is available in Appendix A.

Lenormand et al. (1988) performed physical micromodel experiments and showed dramatically different front configurations occurring when one fluid displaces another in porous media. He divided the front configurations into pure regimes that are modeled by different stochastic techniques. The domains of the stochastic modeling techniques are shown in the phase diagram in Figure 1 (Lenormand, 1987). The phase diagram is applicable to displacement of the wetting fluid by the non-wetting fluid without gravity forces. The pure regimes, labeled DLA, IP, and Anti-DLA, correspond to displacement of a viscous fluid by a non-viscous fluid, capillary displacement, and displacement of a non-viscous fluid by a viscous fluid, respectively. Anti-DLA results in a flat interface

and occurs when the pressure gradient is decreasing in the direction of the flow. The areas between these pure domains are governed by a combination of the applicable forces. The limits of these domains are determined by an evaluation of the capillary pressure at the interface between the two fluids and use the mobility ratio (M) and the microscopic capillary number (Ca) as parameters. The mobility ratio, M , is defined as the ratio of the dynamic viscosity of the displacing fluid and the dynamic viscosity of the displaced fluid. The microscopic capillary number, Ca , is defined as the ratio between the viscous forces and the capillary forces (Lake, 1989).

The phase diagram designates modeling techniques for the pure regimes of capillary and viscous fingering and their limits. Continuum models are in the anti-DLA regime. Most DNAPLs of practical importance are in the transition area based on their viscosity, not in one of the pure domains shown in Figure 2.1. The combined forces acting to stabilize or destabilize the front must be considered to model fluid-fluid displacements between the regimes. The effects of gravity are also important (Wilkinson, 1984; Birovljev et al., 1991) and should be included in determining the NAPL-water front configuration.

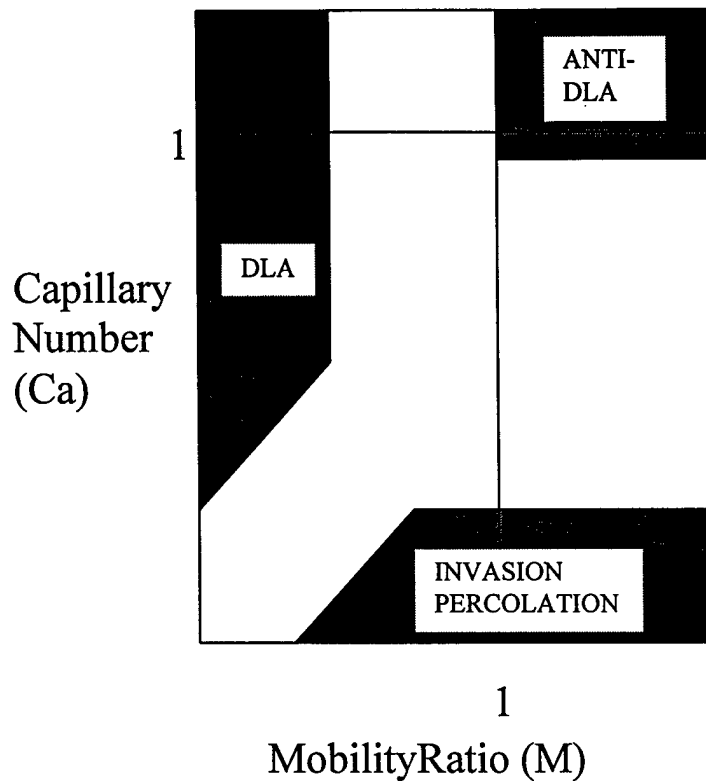


Figure 2.1. The stochastic modeling techniques corresponding to the regimes for which their use is suggested is shown with varying microscopic capillary number and mobility ratio. Adapted from Lenormand's (1987) phase diagram for immiscible fluid-fluid displacement in the absence of gravity.

Several studies have investigated the use of DLA for modeling the displacement of a more viscous fluid by a less viscous one (Paterson, 1984; Chen and Wilkinson, 1985; Maloy et al., 1985; Fernandez et al., 1991; Kiriakidis, et al., 1991) in addition to Lenormand et al. (1988). Paterson (1984) was the first to suggest the application of DLA to fluid-fluid displacements in the absence of gravity. Following Paterson (1984), Maloy et al. (1985) conducted experiments whereby air displaced epoxy in a radial, two-dimensional porous medium. The fractal dimension of the experimental, tree-like structure was the same as that of DLA aggregates. This study showed that DLA could be

used to simulate the displacement of one fluid by another in the limit of an inviscid displacing fluid. In an effort to simulate a broader range of displacing fluids, Kiriakidis et al. (1991) incorporated a sticking probability into the DLA algorithm. Kiriakidis et al. (1991) based the value of the sticking probability on the pressure gradient as calculated by Lenormand et al. (1988) and applied a different sticking probability to each particle depending on whether it represented the wetting or non-wetting fluid. The model simulations of Kiriakidis et al. (1991) are not compared with laboratory experiments. One reason for this may be that the dynamic viscosities corresponding to the simulations are either much lower (7.6×10^{-5} cp) or higher (13 cp) than the majority of NAPLs of interest in contaminant hydrology. With the exception of PCB's, the majority of dynamic viscosities for NAPLs lie in the range of 0.3 cp to 8 cp (Mercer and Cohen, 1990). Fernandez et al. (1991) also changed the probability with which a particle was incorporated into the aggregate. In this study, the "releasing" probability is approximately related to the inverse of the microscopic capillary number through a manipulation of the ratio of pressures (the pressure in the wetting or non-wetting fluid as it relates to the capillary pressure) and an application of Darcy's law in the absence of gravity. As in the case of Kiriakidis et al (1991), the simulations appear to be representative of NAPL-water displacements. It is difficult to evaluate the correctness of this work due to the approximate relationship between the releasing probability and the microscopic capillary number. No evaluation of the microscopic capillary number or any physical fluid properties are given, and hence it is uncertain if realistic fluid pairs will be represented by this determination. In addition, Fernandez et al. (1991) neglects the influence of fluid viscosities (mobility ratio).

CHAPTER 3

MODEL FORMULATION AND CALIBRATION

3.1 Model Formulation

The stochastic aggregation model (SAM) uses a modified DLA algorithm to model the displacement of water by DNAPLs which are more or less viscous than water. Using the model, it is possible to look at the displacement of these fluids under conditions of increasing flow rates and in a gravity field. The front configurations produced under these conditions range from viscous fingers to flat fronts. The model uses macroscopic, dimensionless capillary and bond numbers to circumvent the difficulty of defining parameters on the microscale. An analysis of the stability of the front is followed by an explanation of the stochastic aggregation algorithm and its relationship to the front stability.

3.1.1 Analysis of Front Stability

Instabilities in the fluid-fluid front are likely to arise on the pore scale when a non-wetting fluid invades a wetting fluid in a homogeneous porous medium (Homsy, 1987). Consider a non-wetting fluid displacing a wetting fluid vertically downwards through a homogeneous porous medium. This is shown in Figure 3.1. To initiate flow instability, the interface moves at a pore scale velocity, v , through a distance dz .

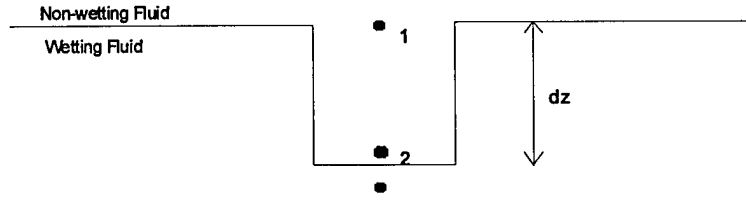


Figure 3.1. Microscopic interface perturbation (adapted from Kueper and Frind, 1988).

The pressures of the wetting phase and non-wetting phases at point 2 are:

$$(P_{nw})_2 = (P_{nw})_1 + \rho_{nw}gz - \frac{\mu_{nw}v dz}{k_{nw}} \quad [1]$$

$$(P_w)_2 = (P_w)_1 + \rho_wgz - \frac{\mu_wv dz}{k_w} \quad [2]$$

where $(P_{nw})_1$, $(P_{nw})_2$, $(P_w)_1$, and $(P_w)_2$ are the pressures in the non-wetting and wetting phases at points 1 and 2. The density and viscosity for each phase are given by ρ and μ , respectively. The third term on the right hand sides of Equations [1] and [2] accounts for the viscous losses as the interface moves from point 1 to point 2. The k in each equation depends on the characteristic length dimension describing the cross section and the shape of the selected dimension representing the pore (Corey, 1994).

The change in capillary pressure between point 1 and point 2, due to the movement of the interface is obtained by subtracting Equation [2] from Equation [1] and rearranging.

$$dP_c = (\rho_{nw} - \rho_w)gz + \left(\frac{\mu_w}{k_w} - \frac{\mu_{nw}}{k_{nw}} \right) v dz \quad [3]$$

If the net capillary pressure is positive, then the small displacement dz will continue to propagate. This leads to a definition of unstable flow for multiphase flow. The flow is unstable if the change in capillary pressure due to displacement dz is positive.

This is analogous to the analysis of Saffman and Taylor (1958) and Chuoke et al. (1959) where the stability of the flow is affected by both the density difference and viscosity difference between the two fluids.

The capillary pressure gradient is given in Equation [4].

$$\nabla P_c = (\rho_{nw} - \rho_w)g + \left(\frac{\mu_w}{k_w} - \frac{\mu_{nw}}{k_{nw}}\right)v \quad [4]$$

A macroscale equation similar to Equation [4] is derived starting with Darcy's law. In immiscible fluid flow, the capillary pressure, P_c , is defined as the difference between the pressure in the NAPL phase and the pressure in the water phase:

$$P_c \equiv P_{nw} - P_w \quad [5]$$

Darcy's law can be written for each phase of a two-phase immiscible system,:

$$q_w = \frac{-kk_{rw}}{\mu_w}(\nabla P_w - \rho_w g \nabla z) \quad [6]$$

$$q_{nw} = \frac{-kk_{nw}}{\mu_{nw}}(\nabla P_{nw} - \rho_{nw} g \nabla z) \quad [7]$$

where w denotes water, nw denotes NAPL, q is the volumetric flux (assumed positive down), μ is the dynamic viscosity, k is the intrinsic permeability, and k_r is the relative permeability for each phase.

The capillary pressure gradient is solved for by combining Equations [5], [6], and [7]:

$$\nabla P_c = \frac{1}{k} \left(\frac{q_w \mu_w}{k_{rw}} - \frac{q_{nw} \mu_{nw}}{k_{rnw}} \right) + \Delta \rho g \sin \alpha \quad [8]$$

where $\Delta \rho = \rho_{nw} - \rho_w$, and α is the angle of the flow from the horizontal. The product of k and k_{rw} is k_w and likewise for the NAPL phase.

Equation [8] is similar to Equation [4]. The factor, $\sin \alpha$, accounts for a reduced gravity effect when the fluid-fluid displacement is not vertical. This term can likewise appear in Equation [4]. The important difference is that Equation [4] is a pore scale equation whereas Equation [8] is a macroscopic equation. Equation [4] describes the change in capillary pressure on a pore scale. The change in capillary pressure on the pore scale directly indicates the stability of the flow in each pore and therefore the movement of the front. Equation [8] has the same form, but the length and the flux are defined on a macroscopic scale, and k is a macroscopic permeability. Equation [8] can be used in the determination of front stability (Hill, 1952; Kueper and Frind, 1988), but using a macroscopic flux in an equation describing microscopic events introduces a scaling factor (Baudet et al., 1986; Oreskes et al., 1994). The experimental work performed by Morrow and Songkran (1981) and Dawson and Roberts (1997) confirm the need for the scaling factor, however neither study has offered an explanation for its derivation or magnitude. One dimensional air-NAPL displacement experiments were performed by Morrow and Songkran (1981) to determine the residual saturation of the nonwetting fluid. The residual saturation was predicted by a linear combination of the microscopic capillary and bond numbers when the capillary number was increased by a factor of 10^4 . By increasing the capillary number by a factor of 10^4 , the capillary and bond numbers were of the same order of magnitude or the capillary number was one order of magnitude

higher than the bond number. In the study performed by Dawson and Roberts (1997), one dimensional DNAPL-water experiments were performed and the DNAPL saturation was predicted by a linear combination of bond and capillary numbers when the capillary number was increased by the inverse of the relative permeability of water. In the case of Dawson and Roberts (1997), the use of the relative permeability as a scaling factor resulted in capillary numbers that were of the same order of magnitude as the bond number or one order of magnitude higher. Both studies applied the linear combination of capillary and bond numbers to an examination of the NAPL residual saturation. Other researchers (Wilson et al., 1990) have used the linear combination in addition to static force balance considerations to estimate NAPL mobility.

The stochastic aggregation algorithm is a pore scale model and the movement of the interface is described by Equation [4]. The problem with using Equation [4] lies in determining the values of pore scale parameters. Instead of estimating pore scale parameters, the scale incongruity is addressed in Equation [8]. A scaling factor of 10^2 was applied to the wetting and nonwetting capillary numbers for the current study. This value was chosen because it yields a capillary number which is of the same order of magnitude, or one order of magnitude higher than the bond number for the chosen nondimensionalization following the results of Morrow and Songkran (1981) and Dawson and Roberts (1997).

The length scale and capillary pressure in Equation [8] are non-dimensionalized with macroscopic parameters following Hilfer and Øren (1996). A hat designates the non-dimensional variables:

$$\hat{\nabla} = \nabla l \quad [9]$$

$$\hat{P} = \frac{P}{P_d} \quad [10]$$

Non-dimensionalizing the capillary pressure gradient results in Equation [11]:

$$\hat{\nabla} \hat{P}_c = \frac{q_w \mu_w l a}{k_w P_d} - \frac{q_{nw} \mu_{nw} l a}{k_{nw} P_d} + \frac{\Delta \rho g l \sin \alpha}{P_d} \quad [11]$$

where a accounts for the change from pore scale to the macroscale and is assigned the value of 10^2 following the discussion on the previous page.

The first two terms in Equation [11] are the macroscopic capillary number for water and NAPL, respectively. The third term is the macroscopic bond number as defined by Hilfer and Øren (1996). Equation [11] is rewritten in terms of these dimensionless numbers.

$$\hat{\nabla} \hat{P}_c = \overline{Ca}_w - \overline{Ca}_{nw} + \overline{Bo} \quad [12]$$

where Ca_w and Ca_{nw} are the capillary numbers for water and NAPL, respectively, and Bo is the bond number. The bars denote that the dimensionless numbers are macroscopic. Equation [12] quantifies the competition between the capillary, viscous, and gravity forces at the interface.

The scaled capillary pressure gradient in Equation [12] is termed the transition number, T , and is grouped as follows:

$$T = (\overline{Ca}_w - \overline{Ca}_{nw}) + \overline{Bo} \quad [13]$$

The first term of the transition number compares the macroscopic capillary numbers for the wetting and non-wetting phases and captures the combined effect of the viscous and

capillary forces. The first term of the equation is positive for NAPLs that are less viscous than water and negative for NAPLs that are more viscous than water. The second term in the transition number is the macroscopic bond number and includes the effects of gravity forces due to the density difference between the NAPL and water. The second term is positive for DNAPLs and negative for LNAPLs, if the NAPL is displacing water from the top.

3.1.2 Stochastic Aggregation Algorithm

The stochastic aggregation model follows a simple algorithm. When the simulation starts, particles are released from a random location opposite the seed point (the location where the DNAPL is injected). The particle has an equal probability of moving up, down, right, or left. If the particle encounters the sides of the network, it “bounces off” and continues walking. The particle continues to walk randomly until it reaches a location adjacent to a location already occupied by a particle. The particle is incorporated into the aggregate with a probability equal to the sticking probability, and a new particle is released. Once incorporated into the aggregate, each particle represents the DNAPL occupying a pore after having displaced the water in the pore. The sticking probability changes the thickness of the branches of the aggregate. The overall density of the aggregate is increased or decreased. This effect is seen by comparing the two simulations in Figure 3.2. The sticking probability for Figure 3.2(a) is 67 percent and the sticking probability for Figure 3.2(b) is 2 percent. The change in aggregate density is a function of the grid size used.

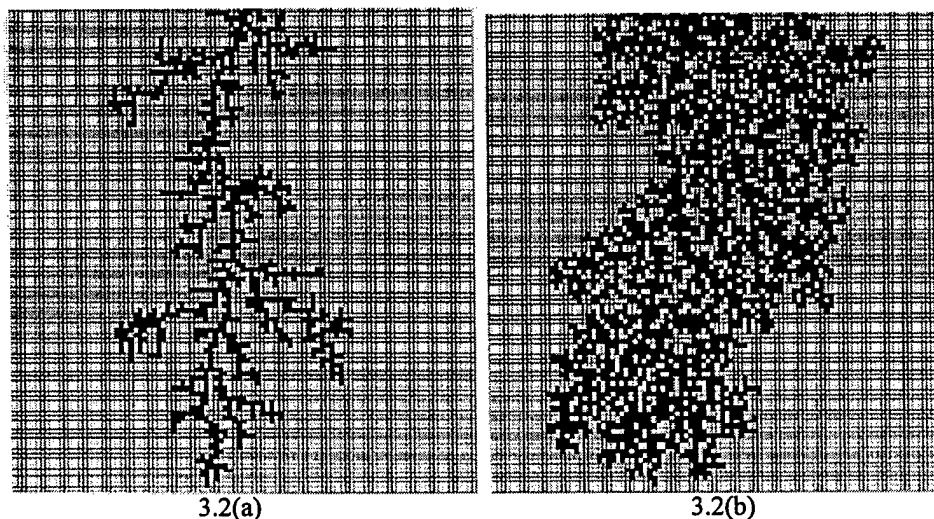


Figure 3.2. Aggregates formed by stochastic aggregation model simulations with different sticking probabilities. The sticking probability for 3.2(a) and 3.2(b) is 67% and 2%, respectively.

The model is calibrated such that the changes in the front stability (viscous fingers to flat fronts) correspond to the changes in the aggregate density as the sticking probability is increased or decreased. The transition number determines the changes in front stability. The transition number is related to the sticking probability via calibration with laboratory experiments.

3.2 Model Calibration

A series of two-dimensional laboratory experiments involving DNAPLs displacing water in a glass bead porous medium were performed at Colorado State University. The flumes were approximately 36 cm in width, 35 cm in length, and 1 glass bead in thickness. A DNAPL was injected into the water-saturated media through a tube at the top of the flume at a constant flow rate. The flow rate and the angle of inclination of the flume from the horizontal were systematically varied. The flux of the DNAPL entering the soil was determined based on the reported flow rate and the area of flow of the tubing used for injection. The cross sectional area of the flume was not used to

determine the flux for the calibration, and neither the flume width nor the tubing width provides the correct dimension for the flux determination. The flume width is an arbitrary dimension that is unknown in a field application of the model; however, the area through which the DNAPL was leaked may be estimated. Each experiment was photographed at different times starting from the time of the DNAPL injection. Carbon Tetrachloride (CTET), 1,2 Dichloroethane (DCA), Tetrachloroethylene (PERC), and Mobile Pyrogard 53 (made by Akzo Nobel, Gallipolis Ferry, WV, under the name Fyrquel 220) were the DNAPLs used in the experiments. The first three are commonly used DNAPLs which are less viscous than water. Mobile Pyrogard 53 is a fire-resistant hydraulic fluid and is more viscous than water.

Collectively, the laboratory experiments show that:

- for a DNAPL which is less viscous than water, the front becomes more unstable as both the NAPL flow rate and the angle from the horizontal are increased.
- for a DNAPL which is more viscous than water, the front becomes more stable as the NAPL flow rate increases, but the front becomes less stable as the angle from the horizontal increases.

The experimental photographs were digitized and analyzed to determine the ratio of DNAPL-occupied area to total area using GLOBAL LAB[®] Image (Copyright © 1995 by Data Translation, Inc., Marlboro, MA), a Windows-based image processing and analysis package. Forty-three laboratory experiments were used to calibrate the model. The calibration group included three different volumetric flow rates (9ml/min, 15ml/min,

and 30 ml/min), where each DNAPL was represented at different angles of inclination. The parameters and pictures for each model calibration case are available in Appendix B.

The stochastic aggregation model was run to determine the average ratio of occupied area to total area for each sticking probability. The model was stopped when the particles reached the bottom of the grid. The grid size was calculated to be 113 X 135, where each grid space represented 1 pore in the experimental photographs. The calibration of the stochastic aggregation model is unique to this grid size. The grid used for the simulations must be square in order to use the graphics program, PSPLOT (written by Kevin Kohler, Nova Southeastern University Oceanographic Center, Dania, FL) to transform the model output. This is a limitation in PSPLOT and not with the model itself. Because of the limitation in the graphics program, a 113 X 113 grid was used. The vertical proportions were kept the same as the laboratory simulations but the sides were truncated. The only laboratory experiments where the DNAPL approaches the sides of the flume are those involving Mobile Pyrogard 53. The model was run 16 times each for 23 sticking probabilities (ranging from $P_s=0.0001$ to $P_s=1$) to determine an area ratio. The area ratio is defined as the average ratio of occupied area to total area for each sticking probability. One simulation runs in 0.5 to 15 minutes (real time) on an IBM RS6000 depending on the value of the sticking probability. The area ratio is a function of the transition number for the laboratory experiments. For the stochastic aggregation model the area ratio is a function of the sticking probability for the selected grid size.

The relationship between the sticking probability and the area ratio for the stochastic aggregation model is shown in Figure 3.3. The data is fit with the following power law relationship:

PAGE 21
IS
MISSING
IN
ORIGINAL
DOCUMENT

model calibration with the laboratory experiments was 0.376, and is on the portion of the curve where a high level of the area ratio's variability is accounted for by the sticking probability.

Equation [14] is rearranged so that the area ratio (AR) is the independent variable.

$$Ps = 1.04323 \times 10^{-3} (AR)^{-2.46323} \quad [15]$$

The AR determined from the photographs of laboratory experiments was used as input to Equation [15] to determine a sticking probability for each photograph. A relationship between the transition number and the sticking probability is then determined by plotting the values for each of the lab experiments in the chosen calibration group. Figure 3.4 shows the relationship between the absolute value of the transition number and the sticking probability as well as the corresponding power law fit. Seven of the laboratory experiments had area ratios that were low enough to yield a sticking probability of greater than one using Equation [15]. These data points are shown on Figure 3.4, but the power law relationship is dotted in this region as the model cannot use a sticking probability greater than one as input. Using the absolute value of the transition number allows the model to use small sticking probabilities to capture phenomena resulting from two different mechanisms. One mechanism is the change in the DNAPL-water displacement resulting from changes in intrinsic permeability within the porous media. The intrinsic permeability (k) may be varied in the calculation of the transition number to account for porous media heterogeneities. Variations in k are included in the comparisons with heterogeneous laboratory experiments in Chapter 5. In this case, a low sticking probability prohibits the particles from entering low permeability regions of the grid. Large values for the transition number are seen when the intrinsic permeability of the

PAGE 23

IS
MISSING
IN
ORIGINAL
DOCUMENT

The sticking probability was calculated for the laboratory experiments not included in the calibration group using Equation [16]. Model simulations corresponding to each of these experiments are discussed in greater detail in Chapter 4.

CHAPTER 4

MODEL CONFIRMATION AND SCALING IN HOMOGENEOUS POROUS MEDIA

Models that attempt to predict natural phenomena are used in every area of science and engineering. The challenge inherent in developing a model to represent real-life processes is in assessing the model's adequacy. The terms verification and validation are often used to make claims of a model's adequacy. Although techniques for verifying and validating models have been developed, it is impossible to truly verify or validate a numerical model for a natural system (Oreskes et al., 1994). Verification of a model is only possible in a closed system in which all system components are established independently. Validation of a model means that the model is legitimate. All input parameters as well as the assumptions used must be known to be accurate to show that a model has been validated.

Even though models cannot be verified or validated, their adequacy must be assessed in some way. The best we can do to assess a model's adequacy is to compare the model results with laboratory or field data and call this process model confirmation. In model confirmation, laboratory or field observations which match model output are said to support the probability that the model has been formulated correctly (Oreskes et al., 1994).

4.1 Model Confirmation

Progress towards model confirmation is accomplished by showing that model realizations match laboratory or field experiments for DNAPL-water displacement. In this chapter, the stochastic aggregation model simulations are compared to two-dimensional laboratory DNAPL-water experiments in homogeneous porous media. In Chapter 5, model simulations are compared with heterogeneous systems.

Model comparisons consist of 33 laboratory DNAPL experiments. The DNAPLs in the validation group are the same as those in the calibration group, however the volumetric flow rates are different. Table 4.1 lists the DNAPL, flow rate, flux, time at which the picture was taken, transition number, corresponding sticking probability, area ratio as calculated from the photographs (AR_1), and the area ratio from the model simulations (AR_2). The area ratio for the model simulations is an average area ratio to within one half of the standard deviation using a 95% confidence interval and 16 model runs. In six of these cases the transition number corresponds to a sticking probability of greater than one. The sticking probability is greater than one when the transition number is less than or equal to 0.205141. This occurs when a combination of a low flow rate and a small angle of inclination from the horizontal yields a low value for the transition number. A sticking probability of one is used in these cases, as an approximation, with good qualitative results. The NAPL did not reach the bottom of the flume in the Mobile Pyrogard 53 laboratory experiments. The volume of DNAPL released is determined to make possible a comparison between the lab experiments and model simulations. The volume is related to a model simulation volume or number of particles based on the

approximate pore size. The model is stopped when the calculated number of particles is incorporated into the simulated aggregate.

Table 4.1
Model Confirmation Cases

DNAPL	Angle	Q (ml min ⁻¹)	q (cm s ⁻¹)	Time (min)	T	Ps	AR ₁	AR ₂
1,2 DCA	90°	3	0.0617	1	0.393	0.423	0.0424	0.0873
1,2 DCA	90°	6	0.1234	1	0.544	0.275	0.0585	0.1040
1,2 DCA	45°	3	0.0617	1	0.322	0.550	0.0731	0.0785
1,2 DCA	45°	6	0.1234	1	0.473	0.331	0.145	0.0965
1,2 DCA	15°	3	0.0617	2	0.214	0.948	0.0804	0.0629
1,2 DCA	15°	6	0.1234	1	0.364	0.467	0.1085	0.0838
CTET	90°	3	0.0617	1	0.313	0.571	0.0644	0.0773
CTET	90°	6	0.1234	1	0.338	0.516	0.1003	0.0805
CTET	45°	3	0.0617	1	0.229	0.866	0.0612	0.0653
CTET	45°	6	0.1234	1	0.254	0.755	0.0986	0.0669
CTET	30°	3	0.0617	2	0.169	1.292 ¹	0.0445	0.0640
CTET	30°	6	0.1234	1	0.194	1.078 ¹	0.0623	0.0640
CTET	15°	3	0.0617	1	0.099	2.608 ¹	0.0275	0.0640
CTET	15°	6	0.1234	1	0.124	1.942 ¹	0.0464	0.0640
PERC	90°	3	0.0617	1	0.354	0.485	0.0551	0.0826
PERC	90°	6	0.1234	1	0.402	0.410	0.0825	0.0883
PERC	90°	12	0.2467	0.5	0.496	0.310	0.0913	0.0990
PERC	45°	3	0.0617	1	0.264	0.715	0.0645	0.0706
PERC	45°	6	0.1234	1	0.312	0.574	0.0636	0.0771
PERC	45°	12	0.2467	1	0.407	0.404	0.1172	0.0889
PERC	30°	3	0.0617	1	0.207	0.991	0.0402	0.0648
PERC	30°	6	0.1234	1	0.248	0.777	0.0344	0.0682
PERC	15°	3	0.0617	1	0.127	1.890 ¹	0.0295	0.0640
PERC	15°	6	0.1234	1	0.174	1.241 ¹	0.0429	0.0640
MP53 ²	90°	3	0.0309	0.08	-2.44	0.0377	0.0060	0.0056
MP53 ²	90°	3	0.0309	0.5	-2.44	0.0377	0.0215	0.0332
MP53 ²	90°	3	0.0309	0.75	-2.44	0.0377	0.0311	0.0498
MP53 ²	90°	3	0.0309	1	-2.44	0.0377	0.0367	0.0665
MP53 ²	90°	6	0.0619	1	-4.98	0.0146	0.0742	0.1329
MP53 ²	90°	6	0.0619	3	-4.98	0.0146	0.2137	0.3987
MP53 ²	45°	3	0.0309	1	-2.47	0.0371	0.0708	0.0665
MP53 ²	45°	6	0.0619	1	-5.02	0.0145	0.0664	0.1329
MP53 ²	45°	6	0.0619	3	-5.02	0.0145	0.1734	0.3987

1. A sticking probability of 1 was used in these cases.
2. In these experiments the DNAPL did not reach the bottom of the flume, and the model was adjusted for the corresponding volume.

The area ratio (AR_1) calculated from the photographs of the laboratory experiments is plotted on the x-axis and the average area ratio (AR_2) from 18 model simulations is plotted on the y-axis in Figure 4.1. Figure 4.1 shows the model's performance in producing simulations wherein the amount of DNAPL in the system at a given flow rate and time may be compared to the laboratory experiments using the value of the area ratio. The data points for Mobile Pyrogard 53 are excluded from Figure 4.1 because their model simulated area ratios (AR_2) were pre-determined. The error bars represent a 90% confidence interval for the model simulations. The data points would lie on the 1:1 line shown on Figure 4.1 if the model simulations matched the experimental photographs perfectly. There is no clear trend indicating that the model consistently over- or under-predicts the area ratio of the laboratory experiments. The variability can be attributed to the error in the conditions under which the laboratory experiments were performed, as well as error in evaluating the area ratio based on the photographs. Using Figure 4.1 as the only means of evaluating the model assumes that both the experiments and the area ratio determination from the photographs are accurate. Figure 4.1 does not give any information regarding the characteristic way in which the DNAPL displaces the water. The characteristic way in which a DNAPL displaces water has been a primary focus of this research and is evaluated by visual comparison.

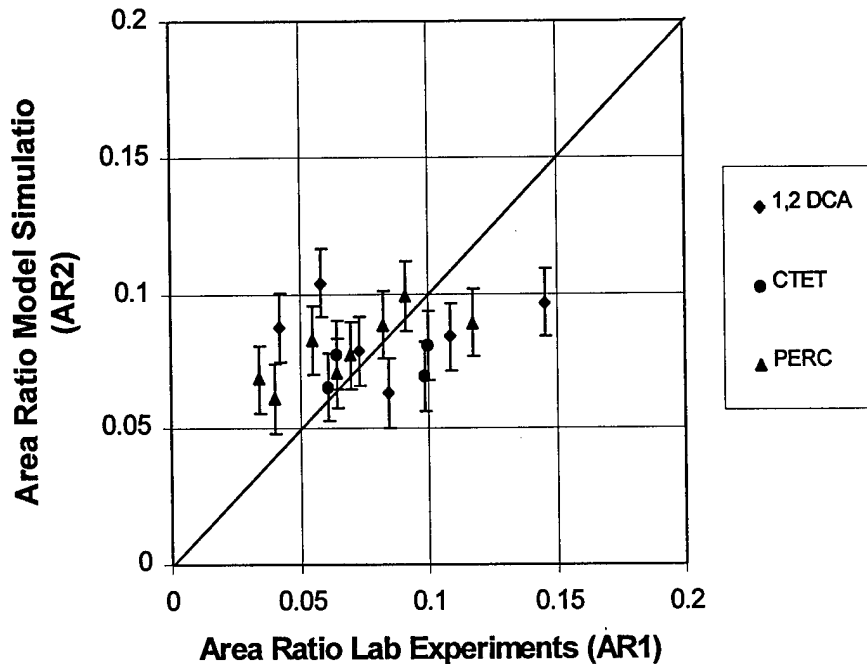


Figure 4.1. A comparison of the area ratios as calculated from the lab experiments and the model simulations.

Two data points furthest from the 1:1 line belong to DCA simulations. For DCA at 90° , 6 ml min^{-1} , and 1 minute (point [0.0585, .01040]) the model predicts a higher area ratio than was observed in the laboratory experiment. For DCA at 45° , 6 ml min^{-1} , and 1 minute (point [0.145, 0.0965]) the model predicts a lower area ratio than was observed in the laboratory. The inconsistency is attributed to the poor contrast of the photographs used in determining the area ratio (see Appendix C). When the contrast of the photograph is poor, the software cannot easily differentiate between areas where the DNAPL is present and darkened areas of the surrounding porous media.

The effects of increasing the flow rate and increasing the angle of inclination are examined for the DNAPLs used in the model confirmation. Increasing the angle of inclination from the horizontal and increasing the flow rate both increase the instability of

the DNAPL-water displacement if the DNAPL is less viscous than water. In the case of a DNAPL which is more viscous than water, increasing the flow rate increases the stability of the DNAPL-water front while an increase in the angle of inclination increases the instability.

Smaller values of the transition number indicate more stable fronts for the range of transition numbers in Table 4.1. This is seen in the case of PERC for two different angles of inclination and a flow rate of 3 ml min^{-1} . At 90° , the value of the transition number is 0.354. With a decrease in the angle of inclination from the horizontal to 15° , the transition number reduces to 0.127. The same trend is seen if the flow rate is changed. For PERC with an angle of inclination of 90° , the transition number increases from 0.354 to 0.402 as flow rate increases from 3 ml min^{-1} to 6 ml min^{-1} .

Whereas DCA, CTET, and PERC are less viscous than water, Mobile Pyrogard 53 is more viscous than water. Because Mobile Pyrogard 53 is more viscous than water, the difference in the viscosities used to calculate the transition number becomes negative. The influence of the flux rate on the magnitude and sign of the transition number is shown by changing the flow rate from 3 ml min^{-1} to 6 ml min^{-1} for Mobile Pyrogard 53 at 90° . The transition number decreases from -2.44 to -4.98 with the increase in flux. The magnitude of T for Mobile Pyrogard 53 is large because of the absolute value of the viscosity difference of 4.86 cP between Mobile Pyrogard 53 and water. The viscosity difference with water ranges from 0.113 cP to 0.035 cP for the other DNAPLs used in the experiments. The increase in the angle of inclination from the horizontal results in larger values of the transition number for Mobile Pyrogard 53. This is seen by looking at Mobile Pyrogard 53 at a flux of 3 ml min^{-1} . The transition number increases from -2.47 to

-2.44 for an increase in the angle of 45° to 90° from the horizontal. This increase is small, but follows the general trend. Tables 1 through 4 in Appendix C contain the input values required for the calculation of the transition number for each case listed in Table 4.1.

The sticking probability approaches positive infinity as positive transition numbers approach zero. This leads to a definition of the model's limits. The sticking probability is greater than one when the transition number is less than or equal to 0.205141. Combinations of inputs resulting in the transition number being less than 0.205141 form a limit for the model's applicability. This limit is encountered in the model validation cases PERC and CTET with of a low angle of inclination and a low flux. The area ratio determined by the laboratory experiment is smaller than the smallest area ratio that the model could provide at a sticking probability of 1. As the absolute value of the transition number goes to infinity, the sticking probability approaches zero. The limit of the model as the transition number increases depends on the amount of time available for a simulation. This is determined by the computer or by physical circumstances.

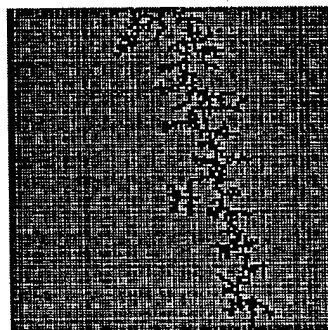
Figures 4.2 through 4.6 show examples of comparisons between the laboratory experiments and the model simulations. A complete set of model validation pictures is shown in Appendix C. Four sets of pictures are shown for DCA, CTET and PERC including pictures at two different angles of inclination and two different inflow rates. Eight pictures are shown for Mobile Pyrogard 53. Four of the Mobile Pyrogard 53 pictures show the model simulations as time progresses for the same angle of inclination and inflow rate. The other four Mobile Pyrogard 53 pictures show changes in the front

with changes in the angle of inclination and inflow rate. It is important to keep in mind that the objective of this type of modeling is not an exact picture of how the DNAPL displaced the water, but a characteristic picture of how the DNAPL displaced the water. Characteristics such as the thickness of a finger, the number of fingers and the relative amount of pore space occupied are important to compare.

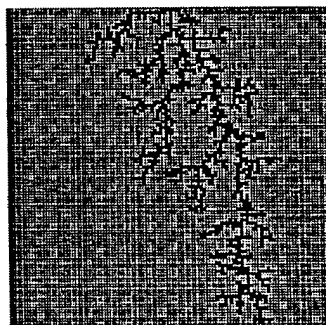
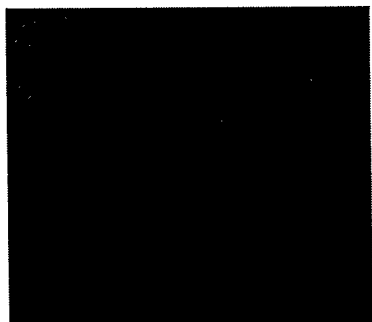
The model simulations and experimental pictures match quite well. In the cases of DCA, CTET and PERC (Figures 4.2, 4.3, and 4.4), the branching and thickness of the fingers are comparable. At 90° and 3 ml min^{-1} the respective DNAPL appears to go straight down through the porous media with little branching. When the flow rate is doubled to 6 ml min^{-1} , more branching can be seen as the DNAPL travels through the flume. As the flow rate increases, the front is increasingly unstable for DCA, CTET, and PERC. Often, increased instability is thought to coincide with thinner, deeper fingers. Both the experimental photographs and the model simulations show that this is not true. The capillary pressure gradient increases as the DNAPL travels deeper, leading to the front becoming increasingly unstable. If the capillary pressure gradient increases, then the capillary pressure at the front must increase as the distance to the front increases. More pores are invaded leading to more lateral movement at higher flow rates as the capillary pressure at the front increases.

In Figure 4.3 for CTET at 15° , the model simulations in (c) and (d) have a sticking probability of one. In both of these cases, the calculated sticking probabilities were greater than one. A sticking probability of one produced model realizations which compare well with the laboratory experiment.

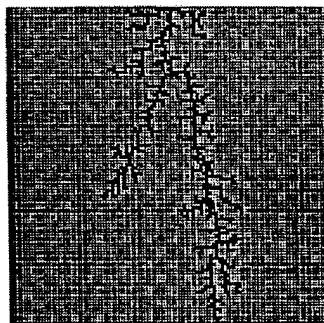
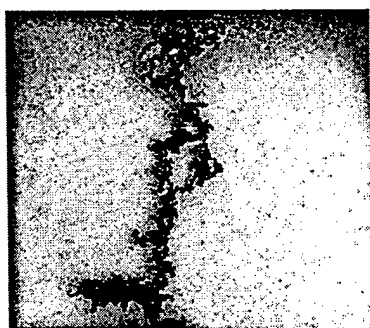
The comparison between the simulations and photographs for Mobile Pyrogard 53 are likewise very good. Figure 4.5 shows Mobile Pyrogard 53 displacing water at 3 ml min^{-1} at 5 seconds, 30 seconds, 45 seconds, and 1 minute. The sticking probability captures the characteristic displacement of the front. The model is stopped when the approximated number of pores are filled based on the volume determination. This does not imply that the model can account for time variation, as there is no time parameter in the equation for the transition number. Other generalized DLA models have incorporated a temporal element into the algorithm (Flury and Fluhler, 1995). The current model can show realizations at different times if the volume is known. Figure 4.6 shows the effect of changing the angle of inclination from 90° to 45° and the flow rate from 3 ml min^{-1} to 6 ml min^{-1} at 1 minute. The Mobile Pyrogard 53 seems to travel farther in the simulation than in the experiment in Figures 4.6(b) and 4.6(d). This is due to the approximation of the number of pores and the pore size. The same size grid is used for all of the model simulations, but the experiments were performed by repacking the flume for each scenario. It is difficult to determine the nature of the packing for each experiment after the fact. The number of particles corresponding to a particular volume is approximated based on an average pore size. Both of these facts contribute to uncertainty in calculating the exact number of particles corresponding to a given volume. This issue will be brought up again in Chapter 5 in regard to natural sands. The transition numbers for Mobile Pyrogard 53 indicate that the DNAPL-water front is stable, as the capillary pressure gradient is negative. The sticking probabilities corresponding to the negative transition number are small leading to model simulations with more compact fronts.



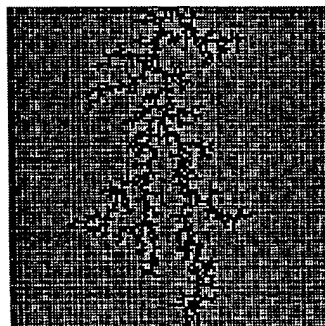
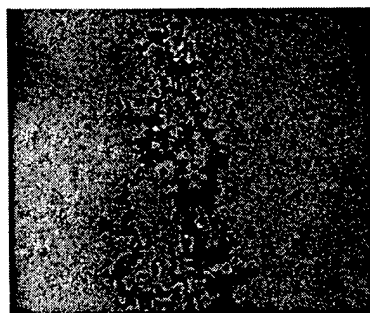
(a) 90° , $Q=3 \text{ ml min}^{-1}$, time=1 min, $T=0.393$, $Ps=0.422$



(b) 90° , $Q=6 \text{ ml min}^{-1}$, time=1 min, $T=0.544$, $Ps=0.275$

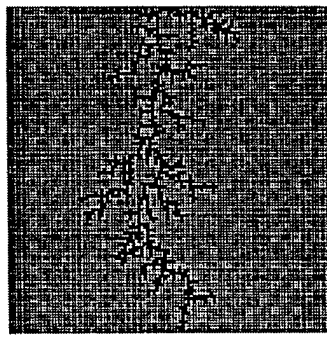
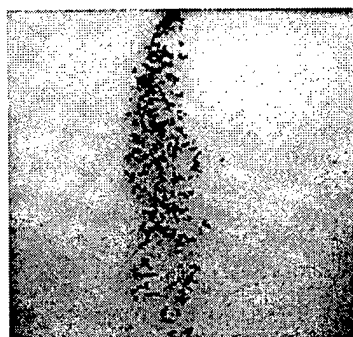


(c) 15° , $Q=3 \text{ ml min}^{-1}$, time=2 min, $T=0.214$, $Ps=0.948$

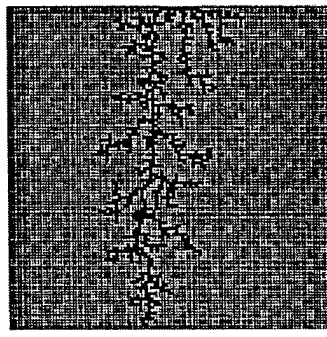
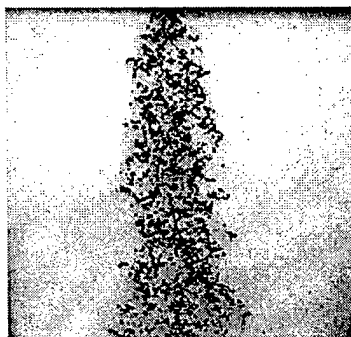


(d) 15° , $Q=6 \text{ ml min}^{-1}$, time=1 min, $T=0.364$, $Ps=0.467$

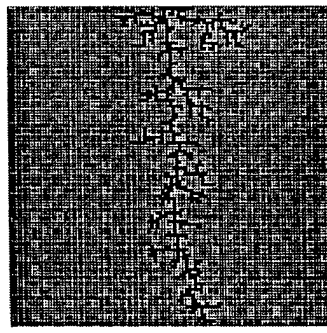
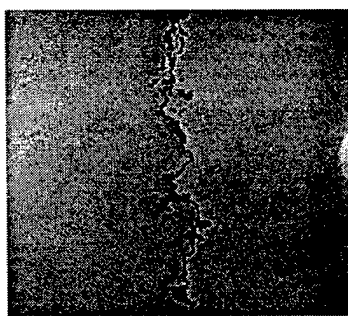
Figure 4.2. Lab experiments and model simulations for 1,2 Dichloroethane (DCA).



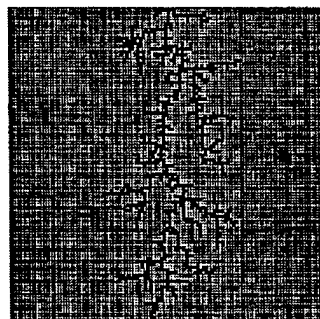
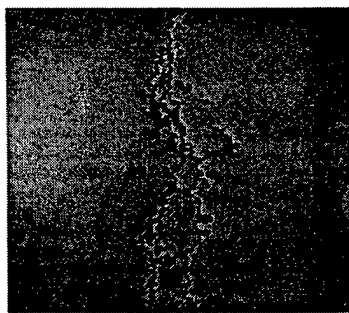
(a) 90° , $Q=3 \text{ ml min}^{-1}$, time=1 min, $T=0.313$, $Ps=0.571$



(b) 90° , $Q=6 \text{ ml min}^{-1}$, time=1 min, $T=0.338$, $Ps=0.516$



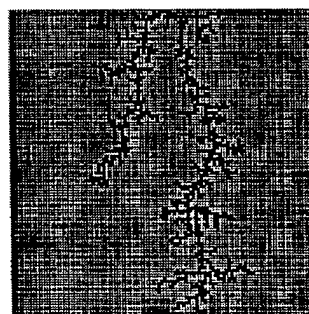
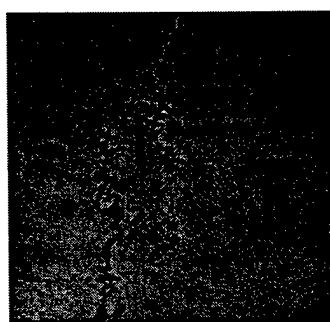
(c) 15° , $Q=3 \text{ ml min}^{-1}$, time=1 min, $T=0.099$, $Ps=2.608^1$



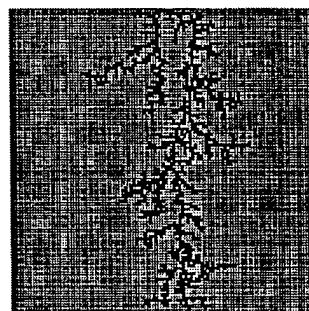
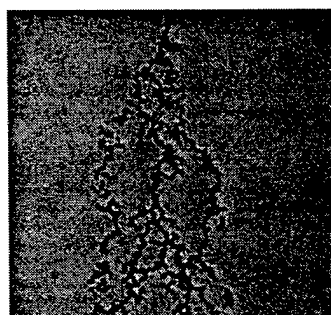
(d) 15° , $Q=6 \text{ ml min}^{-1}$, time=1 min, $T=0.124$, $Ps=1.942^1$

Figure 4.3. Lab experiments and model simulations for Carbon Tetrachloride (CTET).

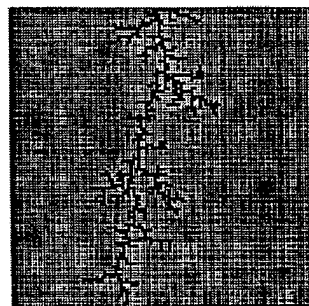
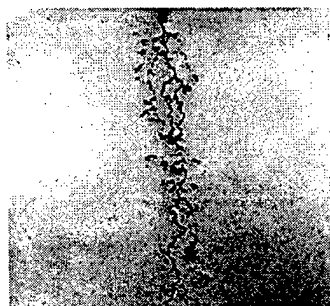
¹Note: A sticking probability of 1.0 was used in the model simulation.



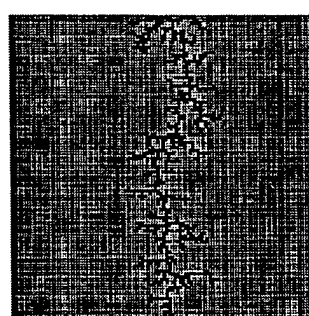
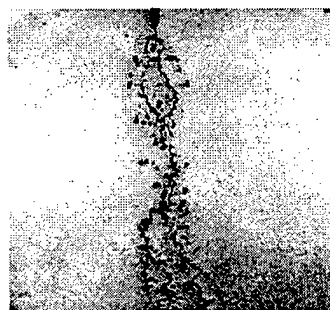
(a) 90° , $Q=3 \text{ ml min}^{-1}$, time=1 min, $T=0.354$, $Ps=0.485$



(b) 90° , $Q=6 \text{ ml min}^{-1}$, time=1 min, $T=0.402$, $Ps=0.411$

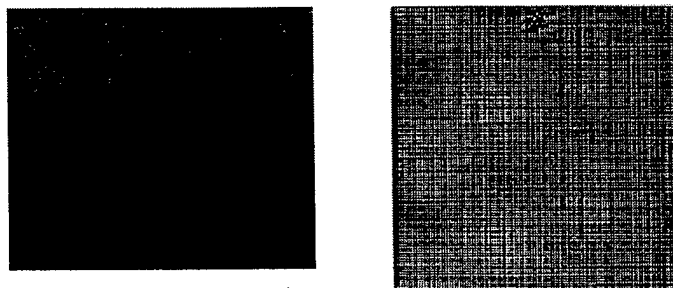


(c) 30° , $Q=3 \text{ ml min}^{-1}$, time=1 min, $T=0.207$, $Ps=0.991$

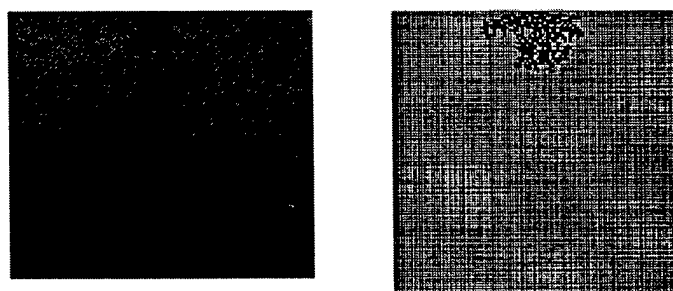


(d) 30° , $Q=6 \text{ ml min}^{-1}$, time=1 min, $T=0.248$, $Ps=0.777$

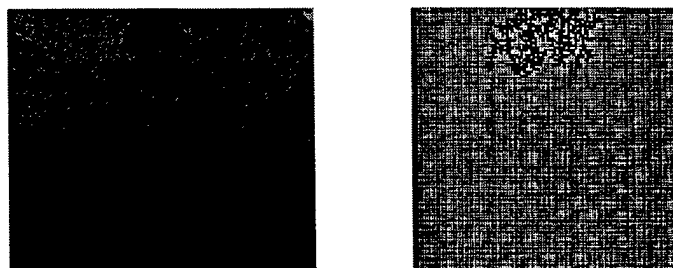
Figure 4.4. Lab experiments and model simulations for Tetrachloroethylene (PERC).



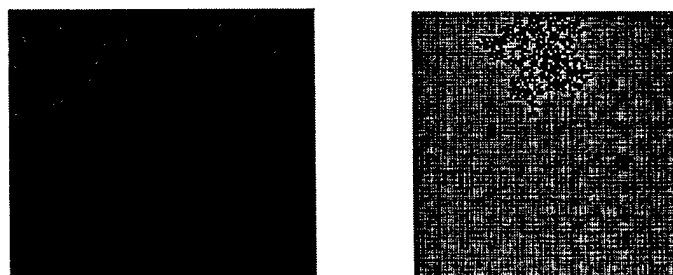
(a) 90° , $Q=3 \text{ ml min}^{-1}$, time=5 s, $T=-2.44$, $Ps=0.0377$



(b) 90° , $Q=3 \text{ ml min}^{-1}$, time=30 s, $T=-2.44$, $Ps=0.0377$

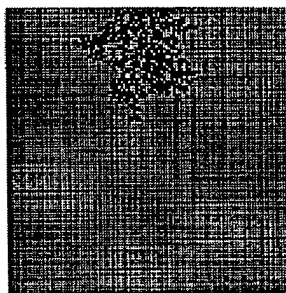
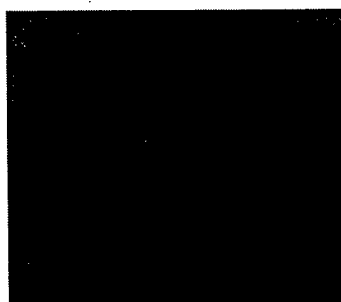


(c) 90° , $Q=3 \text{ ml min}^{-1}$, time=45 s, $T=-2.44$, $Ps=0.0377$

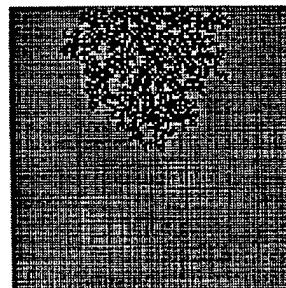
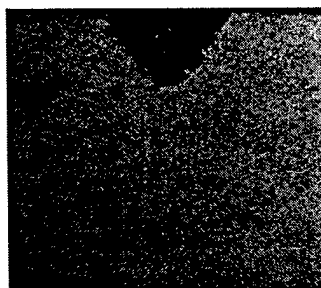


(d) 90° , $Q=3 \text{ ml min}^{-1}$, time=1 min, $T=-2.44$, $Ps=0.0377$

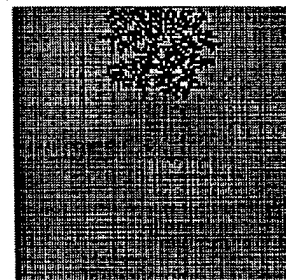
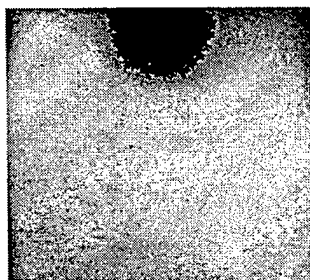
Figure 4.5. Lab experiments and model simulations for Mobile Pyrogard 53 at different times.



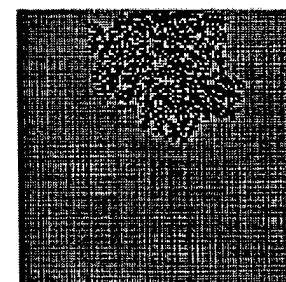
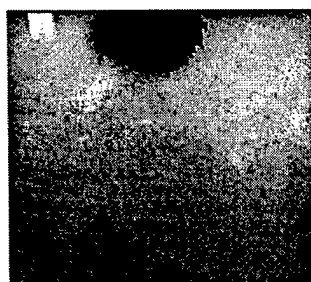
(a) 90° , $Q=3 \text{ ml min}^{-1}$, time=1 min, $T=-2.44$, $Ps=0.0377$



(b) 90° , $Q=6 \text{ ml min}^{-1}$, time=1 min, $T=-4.98$, $Ps=0.0146$



(c) 45° , $Q=3 \text{ ml min}^{-1}$, time=1 min, $T=-2.47$, $Ps=0.0371$



(d) 45° , $Q=6 \text{ ml min}^{-1}$, time=1 min, $T=-5.02$, $Ps=0.0145$

Figure 4.6. Lab experiments and model simulations for Mobile Pyrogard 53.

4.2 Model Scaling

Model confirmation was performed using a grid size corresponding to the approximate number of pores in the flume. The changes in the displacement fronts resulting from changes in flow rate and angle of inclination from the horizontal are apparent even though these flumes were small. Other laboratory experiments found in the literature (Illangasekare et al., 1995 and Kueper and Frind, 1991) used larger flumes, and field spills are at an even larger scale. It is of interest to investigate the scalability of the model.

Grids up to an order of magnitude larger than the model validation simulations are investigated. The area ratio for the model simulations is defined as the number of occupied grid spaces divided by the total number of grid spaces. The area ratio decreases with increasing grid size for the same sticking probability. Figure 4.7 shows the relationship between the area ratio and the grid size for a sticking probability of 0.1. The data result from running the model at each grid size for the given sticking probability. The data points do not reflect an average at the corresponding grid size. The time it takes to complete a simulation increases dramatically as the grid size increases. The simulations generated for model validation on a 113 x 113 grid required a few seconds to 15 minutes (real time) depending on the sticking probability and the user availability on an IBM RS6000. The simulation time increased from 3 minutes for a 200 x 200 to 87 minutes for a 500 x 500 with a sticking probability of 0.1. The simulation using an 800 x 800 grid took approximately 4 days. It is prohibitive to run multiple simulations and produce average area ratios.

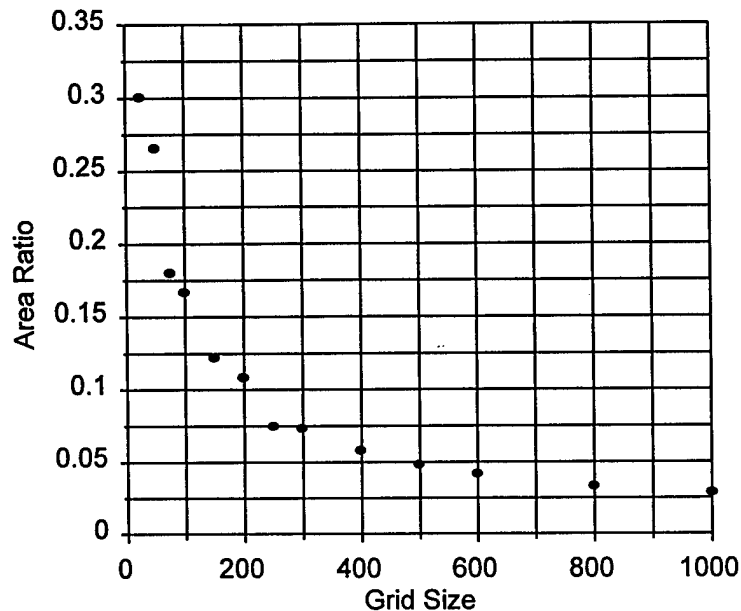
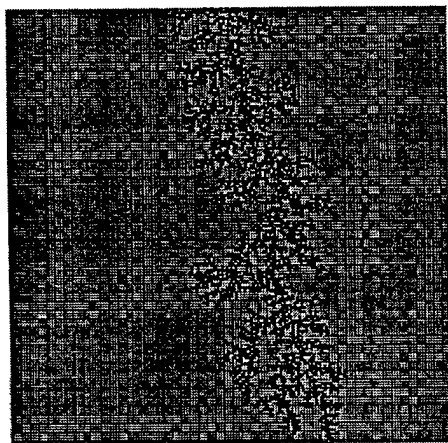


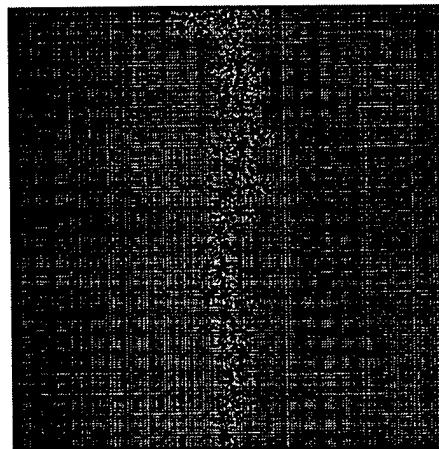
Figure 4.7. The decrease in area ratio with increasing grid size shown for a sticking probability of 0.1.

The change in area ratio with change in grid size does not prohibit the scaling of the model. The characteristics of the aggregate do not change for a given sticking probability even though the relative amount of occupied grid space is changing. This idea is similar to a situation in the field where a DNAPL displaces water in a narrow finger-like pattern. The characteristic of the finger (thickness, branching, etc.) would be the same whether the volume of soil immediately surrounding the finger is considered or a much larger volume is considered. The ratio of occupied pore space to total pore space changes as the selected volume changes. Figure 4.8 shows two model simulations with the same sticking probability ($P_s=0.1$) on different grid sizes. The grid size for 4.8(a) is 200 x 200 and the grid size for 4.8(b) is 600 x 600. Simulations for grid sizes 800 x 800 and 1000 x 1000 were run, but the output cannot be visualized at this time. The darkness of 4.8(b) is due to a limitation in the program used to generate the picture from the

model's output, PSPLOT. The program generates the picture in a space of 4.7 cm by 4.7 cm regardless of the model's grid size. The pictures become darker and darker with the increasing number of lines being drawn in the same space.



4.8(a)



4.8(b)

Figure 4.8. Model simulations for a sticking probability of 0.1. Figure 4.8(a) shows a model simulation on a 200 x 200 grid. Figure 4.8(b) shows a model simulation on a 600 x 600 grid.

The question of model scaling is addressed by determining if the area ratio for a given sticking probability remains characteristically the same. This implies that Figure 4.8(a) has the same area ratio as 4.8(b) if a 200 x 200 portion of 4.8(b) is examined. A smaller sized grid can be used for simulations to show the characteristic DNAPL-water displacement if this is the case. Model simulations with grid sizes ranging over one order of magnitude are examined. The results are presented in Table 4.2 and Figure 4.9. N_p is the number of particles occupying spaces in a 113 x 113 grid centered about the injection point at the top of the grid (the seed particle). The simulations are stopped when the longest finger reached row 113. The area ratio from the larger grid is directly compared to the average area ratio for a 113 x 113 grid at the same sticking probability ($P_s=0.01$).

Table 4.2
Area ratio for a 113 x 113 sub-grid on increasing grid sizes for a sticking probability of 0.01.

Grid Size	N_p	Area Ratio
113 x 113	1854	0.1452
200 x 200	1939	0.1518
300 x 300	1694	0.1327
400 x 400	2339	0.1832
500 x 500	1924	0.1507
800 x 800	2026	0.1587
1000 x 1000	2240	0.1698

Figure 4.9 shows the area ratio oscillating and perhaps increasing slightly over the range of grid sizes investigated. One possible explanation for this occurrence is the increase in lateral grid space. The aggregate ends up with more occupied grid spaces in a given row, increasing the area ratio slightly when there is more lateral space in which the particle can move. This increase is small and results in a 1.35% increase in occupied pore space over an order of magnitude change in grid size. It is concluded from this investigation that the grid may be scaled to the 113 x 113 size used in the model validation with little change to the characteristics of the DNAPL-water displacement in the pore space. This conclusion should be confirmed by studying the grid size and change in area ratio over several orders of magnitude in future studies.

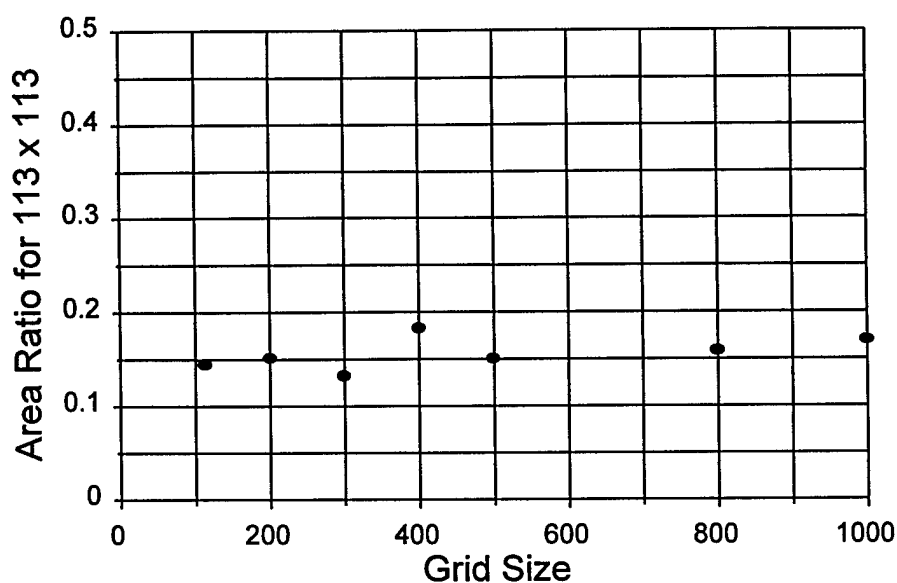


Figure 4.9. The area ratio for a 113 x 113 portion of the simulated grid compared for grid varying sizes up to 1000 x 1000.

The scaling technique is used to evaluate the basic characteristics of larger laboratory experiments and field spills by scaling the DNAPL volume. The volume of Mobile Pyrogard 53 is related to the number of particles in the model simulation in the model validation section. This is accomplished by estimating the percentage of DNAPL occupied pore space using the volume of DNAPL injected and the approximate volume of the pore space. The number of particles necessary for a simulation of a given volume is determined by multiplying the percentage of occupied pore space by the number of pores or grid spaces for the simulation (113^2). This technique is utilized in the simulation of the laboratory experiments of Illangasekare et al. (1995) in Chapter 5.

CHAPTER 5

MODEL CONFIRMATION FOR HETEROGENEOUS POROUS MEDIA

5.1 Heterogeneous Model Confirmation

Heterogenities are incorporated into the model by changing the transition number. In Chapter 4, changes in the transition number corresponding to changes in the sticking probability are explored as a function of the fluid properties (density and viscosity) of the DNAPL and the angle of inclination from the horizontal. The characteristic DNAPL-water front due to porous media heterogenities is explored by changing the values of intrinsic permeability and displacement pressure.

Illangasekare et al. (1995) and Kueper and Frind (1991) carried out DNAPL migration studies in water-saturated heterogeneous porous media. These cases are used for comparison to the stochastic aggregation model.

5.2 Single Fine/Coarse Lens

The experiments by Illangasekare et al. (1995) used a flume measuring 1.22 m wide x 1.83 m high x 0.05 m thick. The flume walls were composed of $\frac{3}{4}$ in. thick plexiglas[®] lined with $\frac{1}{4}$ in. thick tempered glass to allow visualization of the experiment. A steel frame supported the walls. The flume was packed with unconsolidated sands in two configurations. In the first experiment, a 20 cm layer of #70 sand was placed in otherwise homogeneous #30 sand. In the second experiment, a 20 cm layer of #16 sand

was placed in the homogeneous #30 sand. In both cases, the bottom of the #30 or #70 layer was placed 40 cm above the base of the flume. The DNAPL was injected 100 cm above the base of the flume into initially saturated sand. Figure 5.1 from Illangasekare et al. (1995) shows a schematic of the soil configuration.

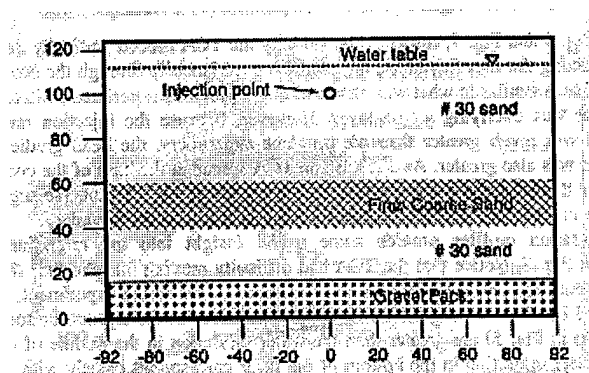


Figure 5.1. The experimental configuration used by Illangasekare et al. (1995).

1,1,1-trichloroethane (TCA) is the DNAPL used in both experiments. TCA has a density of 1.349 g cm^{-3} and a dynamic viscosity of 1.2 cP (Illangasekare et al., 1995).

Table 5.1 shows the displacement pressure, intrinsic permeability, transition number and sticking probability for each soil. The laboratory-scale length of 100 cm and an injection rate of 59 ml min^{-1} are used in the calculation of the transition number.

Table 5.1
Sand characteristics and model parameters for the experiments of Illangasekare et al. (1995).

Soil type	Intrinsic Permeability (cm^2)	DNAPL-water Displacement Pressure (dyn/cm^2)	T	Ps
#16	9.18E-6	3588	-1.58	0.0669
#30	2.26E-6	7791	-3.09	0.0275
#70	2.78E-7	17932	-11.1	0.0051

The same relationship (Equation [16]) is used to relate the sticking probability to the transition number. The size of the grid corresponding to the approximate number of

pores in the flume is estimated to be 2844 pores in height and 4220 pores in width. The model scaling technique discussed in Chapter 4 is used since it is not feasible to run simulations of this size. The grid size for the simulation is the same as the grid size for the model validation, 113 x 113. The grid must be square to use the graphics program, PSPLOT, to visualize the output. The vertical dimensions of the flume from the injection point are scaled onto a 113 x 113 grid due to this limitation and because the flume was packed symmetrically about the vertical centerline. The center of the first row in the grid is used as the seed point corresponding to the injection point. From the top to the bottom of the flume: the first 40 cm layer of #30 sand corresponds to the top 45 rows of the grid, the 20 cm layer of #70 sand corresponds to the next 23 rows of the grid, and the bottom 40 cm of #30 corresponds to the bottom 45 rows in the grid.

The percentage of pore space occupied by the DNAPL is estimated to compare simulations with the physical model results at a given time. The volume of a single pore is calculated as the volume of a sphere with the radius estimated to be twice the radius of a pore neck. The diameter of a pore neck is estimated to be 42% of d_{50} , the average grain diameter (Ng et al., 1978; Pantazidou and Sitar, 1993; Schroth et al., 1995). The number of pores in the flume is approximated by taking the dimension of the flume in each direction and dividing it by grain diameter for the appropriate sand type. The volume of a single pore is multiplied by the total number of pores in the flume. Multiplying the number of pores in each flume dimension and summing these values for each sand type yields an approximate pore volume of 28,600 cm³ for the experiment with the #70 lens and 29,000 cm³ for the experiment with the #16 lens. The percent of DNAPL-occupied pore space is calculated by dividing the volume of DNAPL by the volume of pore space.

The number of particles necessary for a simulation is determined by multiplying the percentage of DNAPL occupied pore space by the number of grid spaces (113^2). Table 5.2 summarizes the model scaling characteristics.

Table 5.2
Model Scaling Characteristics.

	Experiment 1 #70 lens	Experiment 2 #16 lens
Volume of pore space (cm^3)	28,600	29,000
% of TCA occupied pore space at t_1	3.11	4.44
Corresponding number of particles at t_1	397	567
% of TCA occupied pore space at t_2	9.32	10.06
Corresponding number of particles at t_2	1190	1284

Note: t_1 = 15 minutes for Experiment 1 and 30 minutes for Experiment 2
 t_2 = 45 minutes for Experiment 1 and 68 minutes for Experiment 2

Figure 5.2 illustrates the model results for the first experiment. Figure 5.2(a) compares the model simulation with the experiment at 15 minutes. Figures 5.2(b) and 5.2(c) compare two different model simulations with the experiment 15 hours after the spill. In Figure 5.2(b) the simulation contains the volume corresponding to total volume injected. It is more appropriate to compare this simulation with a photograph taken at 45 minutes (the end of injection), but a photograph from that time is not available. The model simulation in Figure 5.2(c) shows fluid redistribution and spreading at the textural interface corresponding to the photograph taken at 15 hours. This is accomplished by using the average residual saturation of 0.3 measured by Illangasekare et al. (1995) to calculate an additional number of particles to release. The area occupied by TCA in

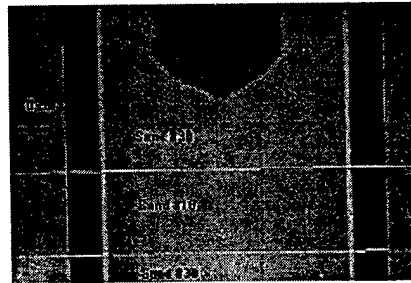
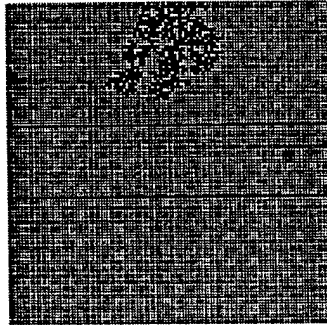
PAGE 48
IS
MISSING
IN
ORIGINAL
DOCUMENT

The model simulations qualitatively match the experimental pictures. Both the computer simulations and the physical model show that the TCA spreads out on the #70 layer. In the experiment, TCA is not able to penetrate this layer because the displacement pressure is not high enough. The lowered sticking probability accounts for this phenomenon in the simulation. Saturations were measured by Illangasekare et al. (1995) using gamma attenuation and show that 41.6 hours after the spill the TCA saturations remain nearly zero in the fine layer. Saturations in the model simulation and experiments are not easily compared as the gamma attenuation system is a point measurement that is not meaningful in the model simulation.

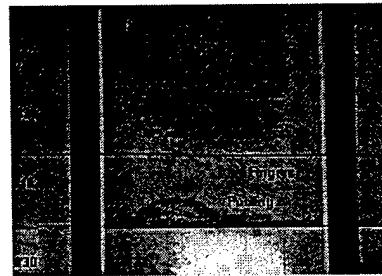
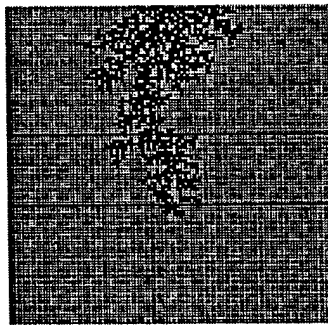
Figure 5.3 shows the results of the model simulation of the second experiment. In this experiment, a coarse layer of #16 sand is sandwiched between layers of #30 sand. Figure 5.3(a) is the DNAPL configuration after the first 30 minutes of injection. Figures 5.3(b) and 5.3(c) show two different model simulations of the same experiment photograph. Figure 5.3(b) shows a model simulation corresponding to the time at which TCA injection stopped (68 minutes). Figure 5.3(c) shows a model simulation where additional particles have been released to account for the fluid redistribution. The experimental photograph in Figures 5.3(b) and 5.3(c) was taken 2 hours after the spill.

A direct comparison between the model simulations and experimental photographs is more difficult for the case of the coarse layer. One problem is that the path the TCA took through the #16 layer is not clearly visible in the photograph in Figures 5.3(b) and 5.3(c). Illangasekare et al. (1995) indicate that fingers were observed in the #16 layer, and the model simulation in Figure 5.3(c) shows that the TCA configuration within the #16 layer is more fingered compared to the configuration in the

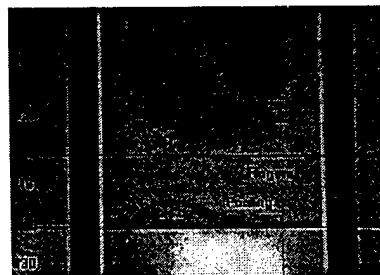
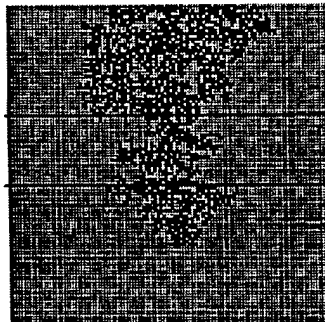
#30 layer. The model simulation in Figure 5.3(c) does not show mounding of the TCA on the lower #30 layer.



5.3(a)



5.3(b)



5.3(c)

Figure 5.3. Model simulation of layered system: #30-#16-#30.

In the first experiment, the sticking probability corresponding to the #70 sand was 0.0051. This is small enough to show particles collecting before eventually sticking in

this region. This does not occur in the model simulation of the coarse layer because the sticking probabilities corresponding to the #30 sand and the #16 sand are relatively large, 0.0275 and 0.0669, respectively. An evaluation of the height of TCA necessary to exceed the entry pressure in the lower #30 layer is missing. This model limitation is discussed in more detail in Chapter 8. The longest finger will continue to grow preferentially until all of the particles have been incorporated into the aggregate without a limitation on particle sticking based on a fluid height.

In summary, the stochastic aggregation model was compared to two heterogeneous laboratory experiments performed by Illangasekare et al. (1995). The simulations were performed on a scaled model grid. Both the grid and the DNAPL volume were scaled. This was done by approximating the percentage of pore space occupied by the DNAPL and allowing the number of particles corresponding to this percentage to form an aggregate on a 113 x 113 grid. A comparison of model simulations and laboratory results is limited to visual similarity for heterogeneous systems (Kueper and Frind, 1991). The stochastic aggregation model shows good agreement to the layered experiments of Illangasekare et al. (1995). A more complex heterogeneous system is considered in section 5.3.

5.3 Heterogeneous Sand Packing

Model simulations are compared to the laboratory experiment performed by Kueper et al. (1989) modeled by Kueper and Frind (1991a and b). In their experiment, tetrachloroethylene (PERC) was allowed to infiltrate into a flume packed with four different sands. The parallel-plate, glass-lined flume was 60 cm high x 80 cm wide x 0.6 cm thick. The flume was packed with four types of sands in the configuration shown in Figure 5.4.

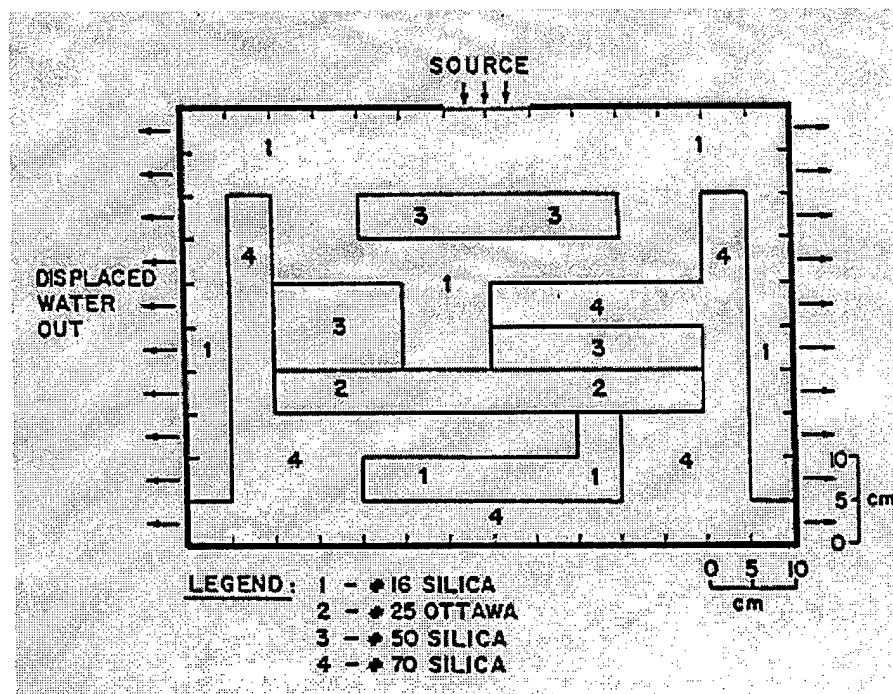


Figure 5.4. The experimental configuration for Kueper et al. (1989).

PERC was injected into the water-saturated sand at the top of the flume. The density and viscosity of PERC is 1.63 g cm^{-3} and 0.9 cP , respectively. The top and bottom of the flume were sealed, except for the injection area shown in Figure 5.4. The sides of the flume allowed the displaced water to escape through a fine wire screen.

The DNAPL infiltrated into the water-saturated flume under a constant head of 4 cm. This corresponds to a transient flow rate at the inflow boundary. A volumetric flow rate is estimated for each of six PERC distributions corresponding to six different times shown in Figure 5.5. The flow rate is estimated by enlarging the pictures for each distribution, graphically estimating the volume, multiplying the volume by the DNAPL saturation given by Kueper and Frind (1991a) as 38%, and then dividing by the time at which the distribution is observed. The flow rates do not vary much given the lack of sophistication of the method. In the order of increasing time the flow rates are estimated to be: $Q_a=0.586 \text{ cm}^3 \text{ s}^{-1}$, $Q_b=0.535 \text{ cm}^3 \text{ s}^{-1}$, $Q_c=0.545 \text{ cm}^3 \text{ s}^{-1}$, $Q_d=0.591 \text{ cm}^3 \text{ s}^{-1}$, $Q_e=0.593 \text{ cm}^3 \text{ s}^{-1}$, and $Q_f=0.578 \text{ cm}^3 \text{ s}^{-1}$.

The size of the grid corresponding to the approximate number of pores in the flume is estimated to be 424 vertically and 593 horizontally. This is based on the size of the #16 sand. The model's grid must be square in order to use the graphics program to visualize the output. This limitation is slightly more complex in this case because the experimental packing of the flume was not symmetric. The vertical dimension of the grid (424) is held constant and the horizontal dimensions are scaled by 71.5%. An additional subroutine is implemented into the stochastic aggregation model containing information on the grid areas corresponding to different sticking probabilities.

The number of particles corresponding to the volume of DNAPL is determined next. The given dimensions for each sand type are multiplied by the porosity of each sand type and added together to estimate the total pore volume. The total pore volume is estimated to be 843 cm^3 . The volume of DNAPL is divided by the estimated volume of pore space to give a percentage of pore space occupied using the average volumetric flow rate and the time. The percent of pore space occupied is multiplied by the grid size

(424²) to obtain the number of particles to be released at each time corresponding to the six diagrams shown in Figure 5.5. Table 5.3 shows the estimated volume of PERC, percent of occupied pore space, and corresponding number of particles for each time.

Table 5.3
Number of particles for model simulation of Kueper et al. (1989).

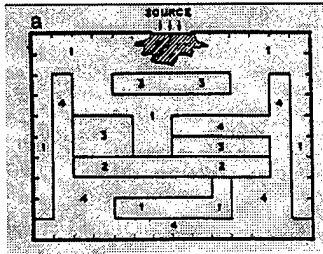
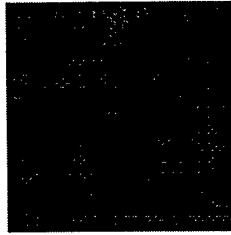
Time (s)	Volume of PERC (cm ³)	% of PERC occupied pore space	Corresponding number of particles
34	19.42	2.3	4140
126	71.98	8.5	15350
184	105.11	12.5	22420
220	125.68	14.9	26800
245	139.96	16.6	29850
313	178.82	21.2	38130

The experiment is modeled twice. In the first set of model simulations, the intrinsic permeabilities and the displacement pressures as reported by Kueper et al. (1989) for each sand are used. Table 5.4 shows the soil properties, transition number and sticking probability for each sand type for the first set of simulations. The laboratory-scale length of 60 cm is used in the calculation of the transition number. Figure 5.5 shows the model simulations and experimental diagrams. Photographs of the experiment were not obtained, but would be preferable for comparison.

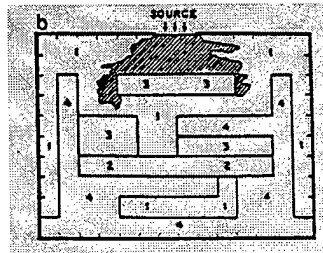
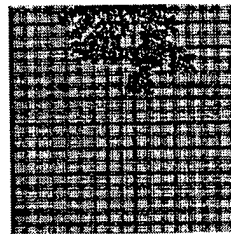
Table 5.4
Sand characteristics and model parameters for simulation #1 of Kueper et al. (1989) experiment.

Soil Type	Intrinsic Permeability (cm ²)	DNAPL-water Displacement Pressure (dyn cm ⁻²)	T	Ps
#16	5E-6	2266	3.16	0.0267
#25	2.1E-6	2663	6.41	0.0104
#50	5.3E-7	8116	8.08	0.00773
#70	8.2E-8	19901	21.05	0.00217

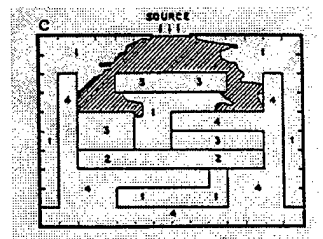
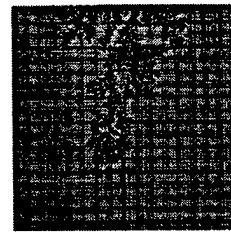
(a) 34s



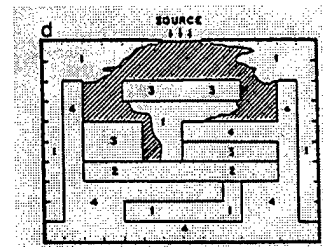
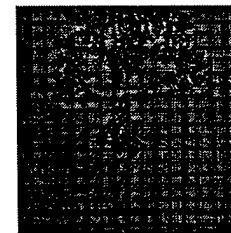
(b) 126s



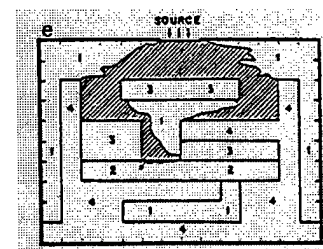
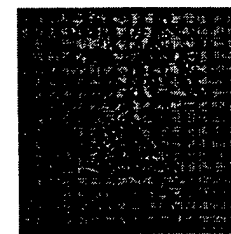
(c) 184s



(d) 220s



(e) 245s



(f) 313s

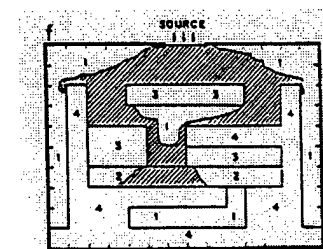
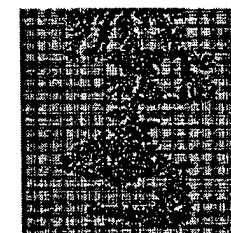


Figure 5.5. Model simulations compared to the experimental results of Kueper et al. (1989).

There is good agreement between the model simulations and the experiment. The comparison is not exact, and there is no reason to believe that an exact comparison is realistic. The model simulations shown in Figure 5.5 resulted from running the model once for the given set of inputs. Likewise, the experimental diagrams show the result of running the physical experiment once. It is arguable that another experimental run would not produce the exact same results even with attention to detail in the packing of the flume and other procedures employed in the experiment. Results refer to the exact pathways taken by the DNAPL, the extent to which the DNAPL travels at a given time, etc. It is reasonable that the same experimental setup and procedures would yield *similar* results. This means that the DNAPL's path would characteristically favor the coarser sands and avoid the finer sands. This is also true of the model. The output of two model simulations run with the same number of particles, corresponding to the same time during the experiment are shown in Figure 5.6. They show characteristically the same DNAPL migration pattern. They are not exactly the same but show that as the DNAPL moves, it characteristically avoids the finest sand and preferentially moves through the coarser sands. The simulations show a realistic DNAPL configuration.

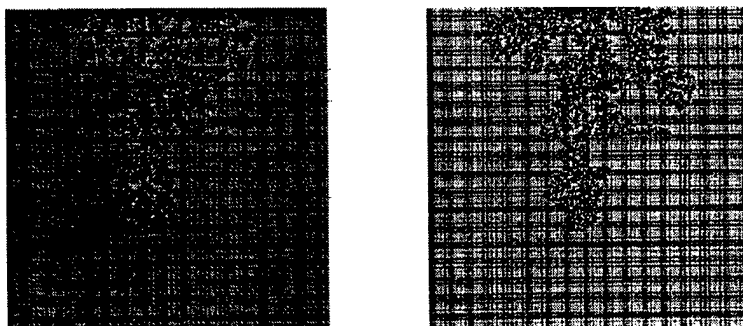


Figure 5.6. Two model simulations run to match the experiment at 184 seconds show characteristically the same DNAPL migration path.

Kueper and Frind (1991a) modeled the experiment of Kueper et al. (1989). Their model results show how the saturations change in a topographic style of output. This information is quantitatively important, but cannot visually demonstrate how the water and DNAPL occupy the pore space.

There are several differences between the model and experimental results. One difference occurs in the top lens marked #3 in Figure 5.4. In the experiment, the PERC avoided this lens and moved around it. The model does not capture this behavior for two reasons. First, the longest finger has the highest probability of growth. There will always be particles which pass through the lens even though the sticking probability for the #3 sand is an order of magnitude lower than that of the #1. As time progresses more and more particles find their way around the #3 lens (compare Figure 5.5(c) to 5.5(d)). The second reason for this difference is that the model does not check the entry pressure to determine if it was exceeded for the #3 sand. This phenomenon was seen in the simulations in section 5.2. Another difference between the experiment and the model simulations is in the depth that the PERC travels. The model simulation shows the PERC traveling farther vertically than in the experiment. The model simulations do not show the same extent of lateral spreading, contributing to this problem. The lack of lateral spreading is due, in part, to not checking the entry pressure. If the model evaluated an entry pressure at the interface between the #1 and #3 sand, particles could not enter the #3 sand until the entry pressure is exceeded. This would lead to more lateral placement of the particles. The crude estimation of the grid size is another possible explanation for the disparity between the model simulations and the experiment. The grid size is estimated by assuming that there is the same number of pores as particles. This assumption relies on an ideal packing. The grid size is calculated based on only one sand

size, the #1 sand, in the simulation of the experiment of Kueper et al. (1989). The #1 sand is chosen because the majority of the DNAPL traveled through the #1 sand. If some combination of the other sand sizes is used, the resulting grid size would be larger because the grain sizes are smaller. Running the simulations on a larger grid would result in shallower vertical extent of the DNAPL. Estimation of the grid size is an area of future research.

The experiment is modeled a second time utilizing the tetrachloroethylene source saturation of 38% used by Kueper and Frind (1991a) in their finite difference model. The saturation is used to calculate the corresponding capillary pressure in the #16 silica sand using the Brooks-Corey (1964) capillary pressure-saturation function given by:

$$S_e = \left(\frac{P_c}{P_d} \right)^{-\lambda} \quad [17]$$

where S_e is the effective saturation, P_c is the capillary pressure, P_d is the displacement pressure, and λ is the pore size distribution. The effective saturation can be calculated given the residual saturation. The residual saturation, displacement pressure, and pore size distribution are given by Kueper et al. (1989). The corresponding capillary pressure, calculated to be 5.03 cm of water, is used in the transition number equation for each of the four sands. The changes in the transition number and consequently the sticking probability, are due solely to the changes in grain size reflected in the intrinsic permeability values. It is necessary to use this capillary pressure for each soil because DNAPL saturation information for each sand is not known. The heterogeneities for this experiment are well defined, but in a field situation the heterogeneities could be statistically characterized with permeability values. Using the permeability information,

the saturation at the injection point, and information on the statistical distribution of the heterogeneities, the transition numbers and sticking probabilities could be calculated. The values of the transition number and sticking probability for each sand type are given in Table 5.5. The model simulations and experimental diagrams are shown in Figure 5.7 for the second simulation.

Table 5.5
Sand characteristics and model parameters for simulation #2 of Kueper et al. (1989) experiment.

Soil Type	Intrinsic Permeability (cm ²)	DNAPL-water Displacement Pressure (dyn cm ⁻²)	T	Ps
#16	5E-6	3027	2.37	0.0389
#25	2.1E-6	3027	5.65	0.0124
#50	5.3E-7	3027	21.65	0.00209
#70	8.2E-8	3027	138.4	0.00018

The simulations (Figure 5.7) match the experimental results more closely than those in Figure 5.5. The sticking probability for the #3 sand is low enough to discourage the DNAPL from passing through the lens. As a result, more particles travel around the lens, filling in the areas where the #1 sand is located. Increased lateral spreading of the DNAPL reduced the depth to which the DNAPL traveled. The DNAPL in the simulations in Figure 5.7 traveled farther than in the physical experiment. This is attributed to the crude grid size estimation. It is important to remember that each simulation is separate when evaluating the simulation pictures. The model does not stop when a certain number of particles is reached, write the output file, and then continue. The model simulation is run for a certain number of particles each time. The simulations show that the model captures the characteristic DNAPL flow path in the same way each time.

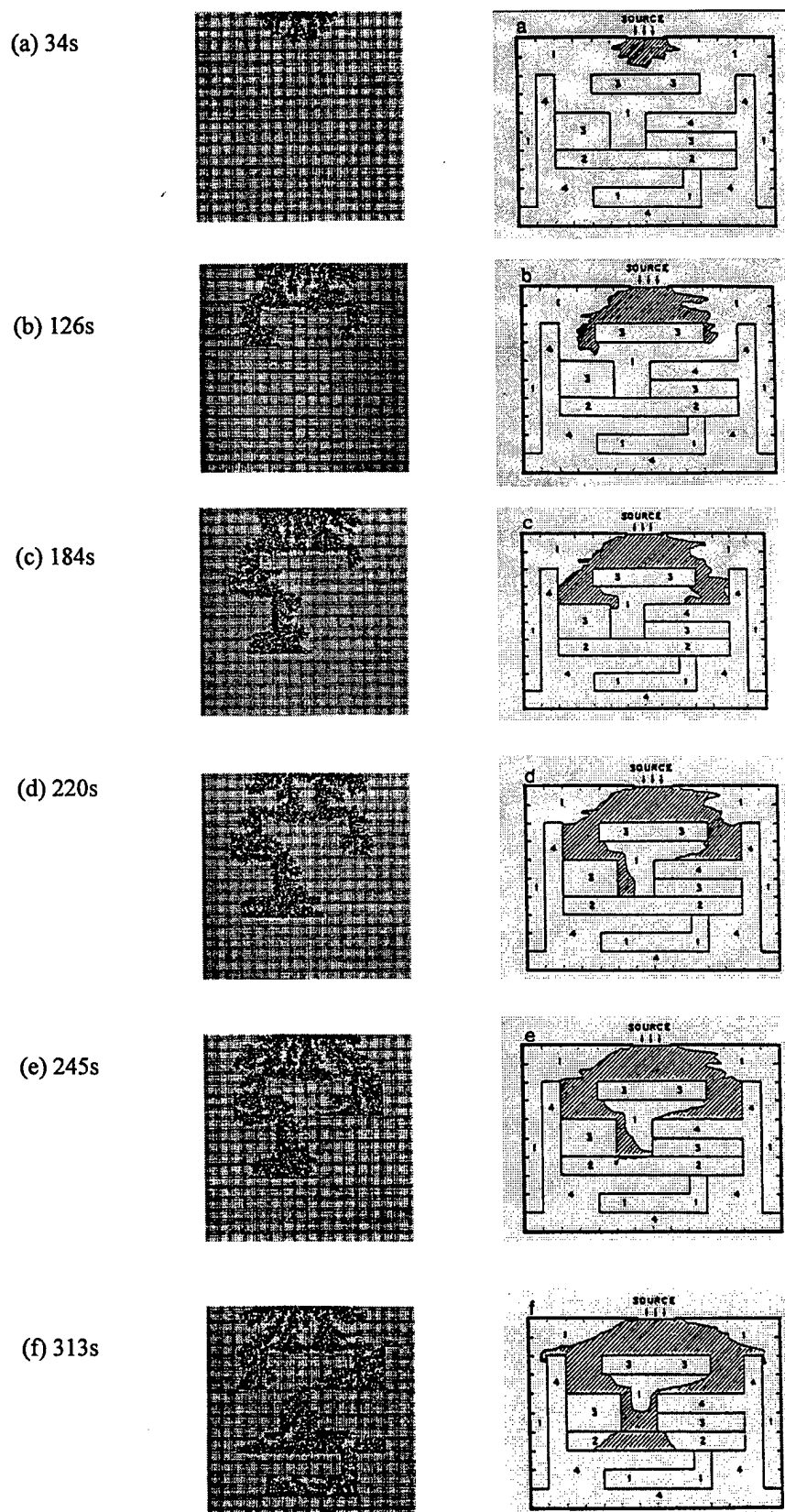


Figure 5.7. Second set of model simulations compared to the experimental results of Kueper et al. (1989).

In summary, the stochastic aggregation model was compared to the heterogeneous laboratory experiment performed by Kueper et al. (1989). The grid size was calculated based on the particle size of the sand used in the experiment. The comparison of the model simulations and the experiment are limited to a visual assessment. While there are some differences between the model simulations and the results of the experiment, the model is able to incorporate a complex array of heterogeneities and show generally the same behavior. Both the experiment and the model simulations were performed only once. It is uncertain that the experiment would yield the same output even if performed in exactly the same way. Likewise the model simulations show only one simulation for each time. Comparing minute details of the simulations with the experiment does not make sense. It is more important to assess whether the model can capture the general behavior of the DNAPL as it displaces water in a heterogeneous porous media.

CHAPTER 6

MODEL DETERMINATION OF BULK RETENTION CAPACITY

Bulk retention capacity, R_s , is defined by Johnson and Kueper (1996) as the average volume of NAPL which is retained per unit volume of the aquifer. The bulk retention capacity differs from the residual saturation of a NAPL in that the residual saturation usually refers to the fraction of pore space occupied by NAPL. The volume of aquifer includes the total volume of soil, gas, and liquid through which the DNAPL migrates. According to the AATDF Technology Practices Manual for Surfactants and Cosolvents: Second Edition (1997), the volume is defined as the "overall volume of medium [and] includes both those lenses and laminations in which residual and pooled NAPL are present and the adjacent lenses and laminations void of NAPL". This concept is useful in providing an estimation of the extent of the contamination in the field. Most DNAPLs have extensive vertical migration patterns similar to the fingers shown in the laboratory experiments in Chapter 3. The bulk retention capacity for a given volume of soil is usually quite small ranging from 0.25 to 3 percent (AATDF, 1997) because of these fingers.

The dilemma encountered in estimating bulk retention capacities lies in the volume determination. The volume as defined by AATDF (1997) is evaluated on a site by site basis and cannot be known with certainty without excavating the DNAPL and soil

at a site. It is useful to estimate the bulk retention capacity using the stochastic aggregation model. Using the model allows a visualization of the occupied pore space, and a variety of “what if” scenarios can be performed. The lab setup of Illangasekare et al. (1995) was chosen to demonstrate the model’s use in determining bulk retention capacities. The bulk retention capacities can be compared relatively. The effect of different soil types (#16, #30, and #70 sand), different DNAPLs, and different flow rates are investigated.

6.1 Retention Capacity Determination

The model simulations in Chapters 4 and 5 show the way in which the DNAPL displaces the water and moves through the soil. The simulated migration patterns are the initial characteristic DNAPL distribution. After the source of DNAPL is stopped there continues to be DNAPL movement and redistribution. This phenomenon was seen by Illangasekare et al. (1995) in the experiments simulated in Chapter 5.

A bulk retention capacity for a specified volume is evaluated by using the model to determine the percentage of pore space affected by the DNAPL and a residual saturation. Anderson (1988) reports that the residual saturation for PERC in saturated coarse Ottawa sand ranges from 0.15 to 0.25. Mercer and Cohen (1990) report the general range of residual saturations for DNAPLs in saturated sand are 0.02 to 0.15. A residual saturation of 0.15 is used for this analysis. Other specified parameters include the length scale of 100 cm and intrinsic permeability values for #16, #30, and #70 sand as measured by Illangasekare et al. (1995). The bulk retention capacity is reported as $L\ m^{-3}$.

Table 6.1 contains the bulk retention capacity calculated for 5 common DNAPLs in three different homogeneous sands at an injection rate of 59 ml min⁻¹. Tables 6.2 and 6.3 contain the bulk retention capacities for the flow rates of 30 ml min⁻¹ and 15 ml min⁻¹, respectively. PERC, CTET, and TCE are evaluated because they are common chlorinated solvents. Creosote is also a common DNAPL and was chosen for its high viscosity. Bromoform was chosen for this example because it is more viscous than water, but not as viscous as creosote. The bulk retention capacities range from 0.62 to 2.86 percent by bulk volume. This is close to the same range reported by the AATDF (1997) of 0.25 to 3 percent by bulk volume.

Table 6.1
Model calculated retention capacity values for Q=59 ml min⁻¹.

Sand	DNAPL	Density (g cm ⁻³)	Viscosity (cP)	Area Ratio	%DNAPL/ Bulk Volume	Retention Capacity (L m ⁻³)
#16	PERC	1.63	0.932	0.3156	1.467	14.67
	CTET	1.58	0.965	0.2852	1.326	13.26
	TCE	1.47	0.560	0.4760	2.213	22.13
	Creosote	1.03	54.0	0.6157	2.863	28.63
	Bromoform	2.9	2.15	0.5349	2.488	24.88
#30	PERC	1.63	0.932	0.4113	1.913	19.13
	CTET	1.58	0.965	0.3813	1.773	17.73
	TCE	1.47	0.560	0.5383	2.503	25.03
	Creosote	1.03	54.0	0.6162	2.865	28.65
	Bromoform	2.9	2.15	0.5751	2.674	26.74
#70	PERC	1.63	0.932	0.5507	2.561	25.61
	CTET	1.58	0.965	0.5365	2.494	24.94
	TCE	1.47	0.560	0.5966	2.774	27.74
	Creosote	1.03	54.0	0.6165	2.867	28.67
	Bromoform	2.9	2.15	0.6066	2.821	28.21

Table 6.2
Model calculated retention capacity values for $Q=30 \text{ ml min}^{-1}$.

Sand	DNAPL	Density (g cm^{-3})	Viscosity (cP)	Area Ratio	%DNAPL/ Bulk Volume	Retention Capacity (L m^{-3})
#16	PERC	1.63	0.932	0.2186	1.016	10.16
	CTET	1.58	0.965	0.1948	0.906	9.06
	TCE	1.47	0.560	0.3799	1.766	17.66
	Creosote	1.03	54.0	0.6146	2.858	28.58
	Bromoform	2.9	2.15	0.4601	2.139	21.39
#30	PERC	1.63	0.932	0.3039	1.413	14.13
	CTET	1.58	0.965	0.2735	1.272	12.72
	TCE	1.47	0.560	0.4690	2.181	21.81
	Creosote	1.03	54.0	0.6156	2.863	28.63
	Bromoform	2.9	2.15	0.5318	2.473	24.73
#70	PERC	1.63	0.932	0.4894	2.275	22.75
	CTET	1.58	0.965	0.4658	2.166	21.66
	TCE	1.47	0.560	0.5742	2.669	26.69
	Creosote	1.03	54.0	0.6164	2.866	28.66
	Bromoform	2.9	2.15	0.5950	2.767	27.67

Table 6.3
Model calculated retention capacity values for $Q=15 \text{ ml min}^{-1}$.

Sand	DNAPL	Density (g cm^{-3})	Viscosity (cP)	Area Ratio	%DNAPL/ Bulk Volume	Retention Capacity (L m^{-3})
#16	PERC	1.63	0.932	0.2186	0.691	6.91
	CTET	1.58	0.965	0.1948	0.621	6.21
	TCE	1.47	0.560	0.3799	1.260	12.60
	Creosote	1.03	54.0	0.6121	2.846	28.46
	Bromoform	2.9	2.15	0.4601	1.614	16.14
#30	PERC	1.63	0.932	0.3039	0.950	9.50
	CTET	1.58	0.965	0.2735	0.844	8.44
	TCE	1.47	0.560	0.4690	1.708	17.08
	Creosote	1.03	54.0	0.6144	2.857	28.57
	Bromoform	2.9	2.15	0.5318	2.113	21.13
#70	PERC	1.63	0.932	0.4894	1.831	18.31
	CTET	1.58	0.965	0.4658	1.688	16.88
	TCE	1.47	0.560	0.5742	2.461	24.61
	Creosote	1.03	54.0	0.6161	2.865	28.65
	Bromoform	2.9	2.15	0.5950	2.651	26.51

6.2 Changes in Bulk Retention Capacity with Varying Parameters

The bulk retention capacities calculated by the model are investigated with the variations in flow rate, intrinsic permeability, and viscosity. Figure 6.1 shows the bulk retention capacity increasing as the flow rate increases for #30 sand. As the flow rate increases, the DNAPL configuration progresses from single fingers to multiple fingers and the DNAPL occupies more of the area. The model accounts for the increased amount of area occupied by the DNAPL without generalizing the area due to the increase in lateral spreading of the DNAPL. The retention capacity for creosote does not show as dramatic an increase as the other DNAPLs, due to its high viscosity. The data for each DNAPL in Figure 6.1, including creosote, can be modeled using varying coefficients of a simple logarithmic equation, $R_s = a + b \ln(Q)$, where a and b are empirical coefficients determined for each fluid.

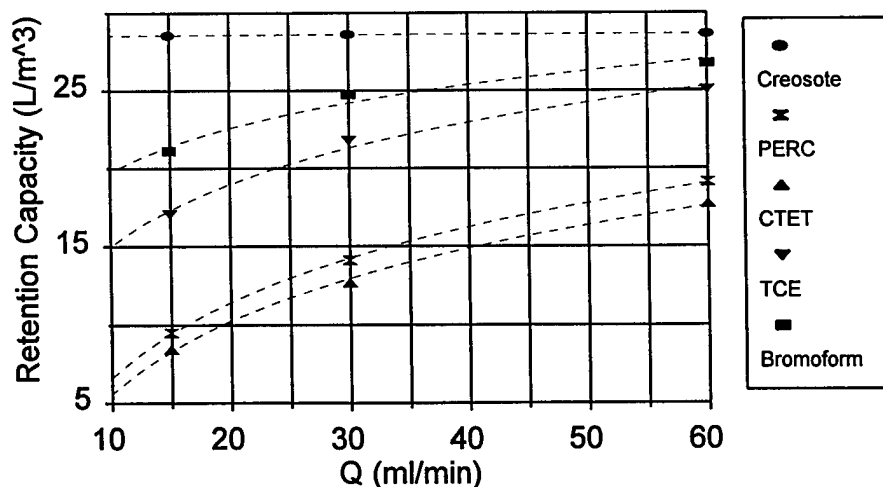


Figure 6.1. The bulk retention capacity increases as the flow rate increases for 6 common DNAPLs.

Figure 6.2 shows the change in bulk retention capacity with the change in intrinsic permeability for a flow rate of 30 ml s^{-1} . The other flow rates show similar trends. The bulk retention capacity decreases as the intrinsic permeability increases. As fluids invade finer sands, the capillary forces have increasing influence over fluid movement, and the fluid spreads laterally leading to a greater amount of entrapment (Morrow and Songkran, 1981). The amount of entrapped fluid (residual saturation) remains the same (15%) for this example. Figure 6.2 shows the influence of the increased spreading due to the changing intrinsic permeability. The data points for creosote appear to form a straight line, but in fact follow the same trend as the other DNAPLs. The curves in Figure 6.2 for each DNAPL can be modeled with a simple power fit, $R_s = a (k)^b$, with empirical coefficients, a and b changing for each DNAPL.

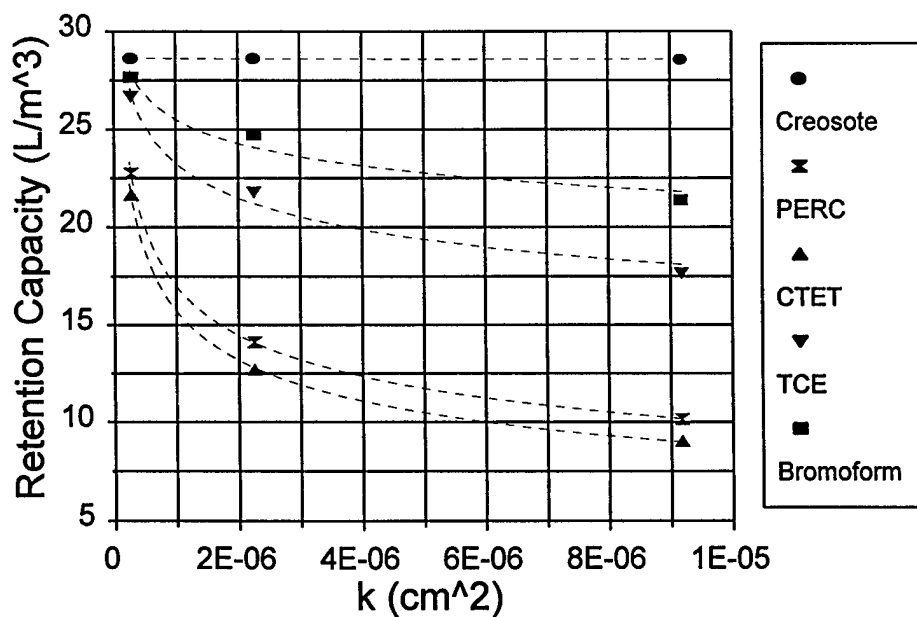


Figure 6.2. The bulk retention capacity decreases as the intrinsic permeability increases for 6 common DNAPLs.

Figures 6.3 and 6.4 show the relationship between the bulk retention capacity and viscosity difference for each type of sand. The viscosity difference between the DNAPL and water increases as the bulk retention capacity increases until the bulk retention capacity approaches 29 L m^{-3} . In Figure 6.4, the data points corresponding to creosote are excluded to show the increasing part of the curve. Figures 6.3 and 6.4 show that fluids with high viscosity differences relative to water, such as creosote, have higher retention capacities. The influence of different intrinsic permeabilities is also seen in these figures. The values corresponding to the finest sand (#70) have the highest retention capacities for the same DNAPL. The data can be modeled by a modified exponential function of the form, $R_s = a(b - e^{-cu})$, where a , b , and c are empirical coefficients determined for each sand type.

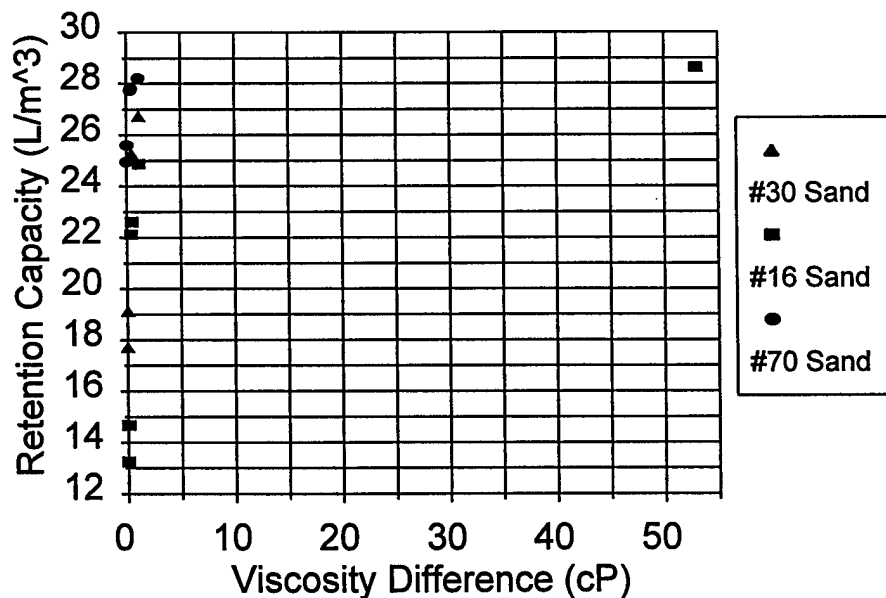


Figure 6.3. The bulk retention capacity approaches 29 L m^{-3} with increasing viscosity difference relative to water.

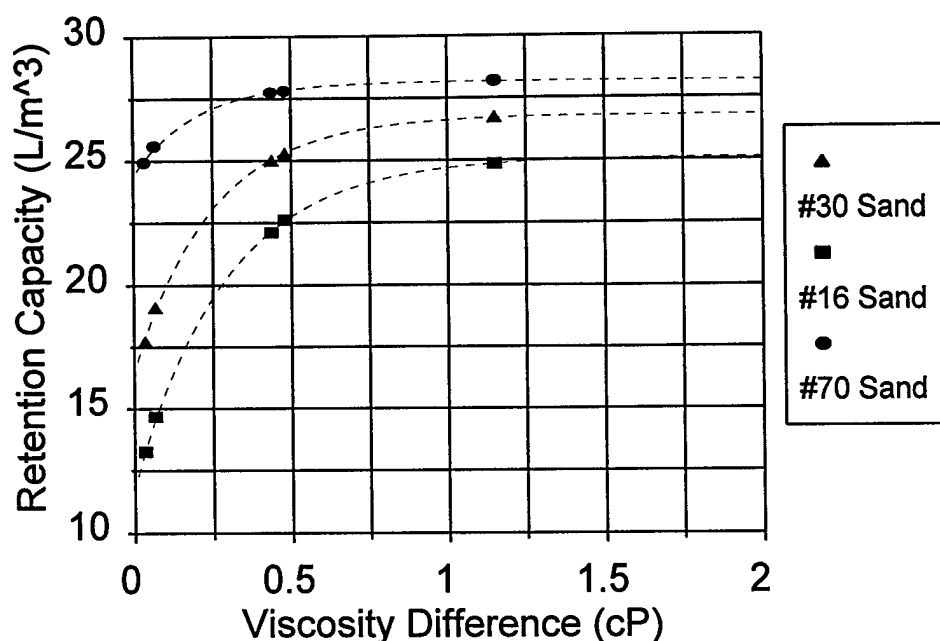


Figure 6.4. The portion of Figure 6.3 with viscosity differences ranging between 0 and 2.

Changes in bulk retention capacity with changes in flow rate, intrinsic permeability, and viscosity are easily assessed by using the model. As the flow rate is increased the bulk retention capacity increases logarithmically. This is attributed to a higher capillary pressure gradient yielding more pores accessible for displacement. The bulk retention capacity increases according to a modified exponential function as the viscosity difference increases. A limit of 28.7 L m^{-3} is approached for the bulk retention capacity in both cases. This is an artifact of the bulk volume chosen. If the chosen bulk volume is greater, the corresponding model grid will be bigger and the retention capacity reaches a smaller limit. The DNAPL remains in 2.87% of the bulk volume in the limit of very high flow rate or very large viscosity difference. This corresponds to the DNAPL traveling through 61% of the pore space with a residual saturation of 15%. Figure 6.5

shows a model simulation where the DNAPL injected from a point source, traveled through approximately 61% of the pore space in the given volume.

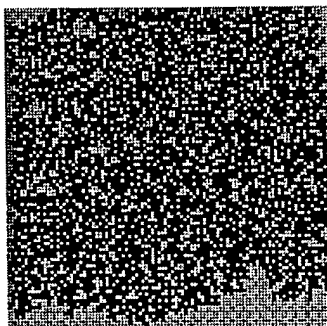


Figure 6.5. A DNAPL occupying 61% of the pore space.

The model is also used to investigate the effect of changing intrinsic permeability on the bulk retention capacity. In this case the bulk retention capacity decreased with increasing permeability reaching a limit dependent on the DNAPL's viscosity and density properties.

In summary, changes in bulk retention capacity with changing fluid and soil properties are useful for field scale determinations. The stochastic aggregation model can be used for this purpose. The bulk retention capacity can be approximated and a visualization of the way in which the DNAPL initially occupied the soil is useful in characterizing the source zone. Varying parameters to determine a range of values corresponding to differing scenarios due to the uncertainty in parameter values is easily accomplished.

CHAPTER 7

MODEL EVALUATION

The benefits and limitations of the stochastic aggregation modeling approach are explored in this chapter.

7.1 Benefits of the Stochastic Aggregation Model

The stochastic aggregation model can visually simulate the characteristic unstable flow patterns seen in DNAPL-water displacement in porous media. The objectives defined during the formulation of the model included linking the DLA aggregate growth to the front instability, exploration of the model to show trends in DNAPL migration with changing fluid properties and buoyancy, incorporation of porous media heterogeneities, determination of bulk retention capacity values, and comparison with lab experiments. These objectives were satisfied. Further exploration of the model will satisfy larger and arguably more relevant field scale objectives.

The stochastic aggregation model allows the user to visualize the migration pattern of a DNAPL traveling through water-saturated porous media at the pore scale. The migration pattern is based on the porous media and DNAPL properties including intrinsic permeability, displacement pressure, inflow rate, DNAPL density and DNAPL viscosity. The model does not generate a unique DNAPL configuration for a given set of inputs because random numbers are used to determine the placement of particles on the

grid. The model simulations show characteristic DNAPL configurations. The important information from the model realizations is the characteristic DNAPL migration pattern (fingering or flat front) and the relative amount of pore space occupied as the DNAPL migrates through the soil. The relative amount of pore space occupied by the DNAPL is correlated to the model inputs for a given grid size and remains constant for those inputs. More realistic source zone configurations are the ultimate goal of the model simulations.

The stochastic aggregation algorithm is simple. Complex numerical modeling techniques are not needed. Model simulations run in less than 15 minutes for sticking probabilities as small as 1×10^{-3} at a grid size of 113×113 . The time necessary to run simulations increases dramatically with increasing grid size. It was shown that over an order magnitude increase in grid size, the characteristics of the aggregate on a given scale remain the same, and allow a smaller grid to be used.

Heterogeneities are easily incorporated into the model. Different areas of the grid are assigned different sticking probabilities corresponding to changes in the soil parameters. Comparisons between model simulations and the experiments of Illangasekare et al. (1995) and Kueper and Frind (1991) show good agreement. This is the first study of a stochastic aggregation algorithm based on DLA that is compared to physical experiments.

The model is used to calculate bulk retention capacities. Results of simulations in this study are within the range of retention capacities seen in field experiments (Poulsen and Kueper, 1992) and cited by others (AATDF, 1997). The value of the model is that in addition to a relevant bulk retention capacity, a graphic of the DNAPL migration is also available. Using the model to determine bulk retention capacities allows for "what

if" scenarios to be run in field situations where parameters may not be known with certainty. Other methods of calculating and/or measuring bulk retention capacities in the field include the use of partitioning tracers. Partitioning tracers yield a field-scale bulk average NAPL saturation. It is possible to use this field-measured value to back-calculate a sticking probability. The sticking probability may then be used as model input to create a visualization of the characteristic DNAPL-water displacement.

7.2 Limitations of the Stochastic Aggregation Model

Many limitations of the stochastic aggregation model have been discovered during the course of this research. This is expected when using a relatively new technique. Some limitations are interesting in that they are unique to this modeling technique.

The lack of theory between DLA-type models and fluid-fluid displacement remains the largest detriment to the modeling technique. The formulation of the model is based on a calibration of the numerical description of the stability of the front (T), as it is influenced by the fluid and porous media properties, to the sticking probability in the model. In this first attempt, the author calibrated the model using a set of laboratory experiments instead of taking on the problem of establishing the theoretical link. The general lack of other DNAPL experiments and their varying laboratory procedures made broad model calibration difficult. The lack of theory pertains to the relationship between the sticking probability and the physical parameters governing the movement of the DNAPL as it displaces water. This link was investigated in the past in the absence of gravity (Fernandez et al., 1991; Kiriakidis et al., 1991) but has not before been linked to

the Saffman and Taylor (1958) and Chuoke et al. (1959) equation describing the instability of the front. Until the mathematics describing the aggregate growth as a function of a changing sticking probability are determined, the theoretical link cannot be established.

Time is not incorporated into this stochastic aggregation model. The model is only applicable to steady flow conditions at the inflow boundary. The model simulates DNAPL-water displacement at varying times if the volume of DNAPL present at the time in question is known. If the volumetric flow rate does not change substantially there is good agreement between the model simulation and the experiment. Other researchers (Flury and Fluhler, 1995) have devised time aspects into modified DLA algorithms. This is an area for future expansion of the stochastic aggregation model.

The model does not determine the capillary pressure during a model simulation when varying soil properties are incorporated into the grid. The displacement pressure is used in the determination of the transition number, and it provides general information about the porous media. In this capacity it does not ensure that the aggregate generated by the model will grow in such a way that areas of the porous media having high entry pressures will not be invaded. An entry pressure incorporated into the model would allow the model simulations to be more realistic. The aggregate would tend to grow preferentially along (lateral to) a layer of lower permeability by applying the entry pressure as a constraint on the addition of particles to the aggregate. The same volume of DNAPL would not travel as deep with more lateral spreading.

There are cases of DNAPL-water displacement that are beyond the limits of the model as determined by the model calibration and cannot be simulated. Combinations of

parameters resulting in transition number values lower than 0.205141 result in a sticking probability greater than one. One is the largest sticking probability that can be used in the model. Each sticking probability corresponds to an area ratio given by Equation [15]. The cases where the sticking probability is greater than one result in configurations where the area ratio is less than the smallest sized finger the model can generate. The model validation cases of CTET and PERC at 15° are included to show that using a sticking probability of one works reasonably well in these cases.

Simulations on very large grids (larger than 1000×1000) are not feasible due to large computational time requirements. A simulation run with a sticking probability of 0.8 took 22 hours of real time and 730 minutes of CPU time (IBM RS6000) on a 1000×1000 grid. There are some interesting questions that could be investigated if it were easier to run larger problems. One such question was encountered during the evaluation of the model scaling. It is not clear whether or not the area ratio determined for a set grid size and a given sticking probability increases with grid sizes larger than 1000×1000 . This is an important consideration if the model is to be used on field scale cases where there could conceivably be grid sizes of $10^6 \times 10^6$ or larger.

The current model performs two-dimensional simulations. It is straight forward to design a similar algorithm in three dimensions. A three-dimensional algorithm requires a theoretical link between the sticking probability and the physical parameters. This is due to a lack of three-dimensional experiments available for calibrating the model.

The graphics program used to generate a post script file for the model's output limits the visualization of the output. This is not a limitation with the model itself, but of the program entitled PSLOT. PSLOT was obtained with written permission from

Kevin Kohler, Coordinator of Computing Services at Nova Southeastern University Oceanographic Center, Dania, FL. The code is written in Fortran 90 and is a powerful and extensive program. PSPLOT shows the model's output on a square grid of specified size. The size of the picture output by PSPLOT remains the same regardless of the grid size. This is a drawback because more and more lines are drawn in the same amount of space as the grid size increases. The pictures become darker and darker. The resulting graphic is completely black at a grid size of 800 x 800.

This modeling technique shows promise. This is evidenced by the close matching of the model simulations with the laboratory experiments. This model, however, is new and the limitations outlined above need to be addressed.

CHAPTER 8

SUMMARY, CONCLUSIONS, AND RECOMMENDATIONS

The objectives of this research were to model DNAPL migration in saturated porous media at the pore scale, evaluate the modeling technique through comparisons with DNAPL-water displacement studies in homogeneous and heterogeneous porous media, and to investigate the application of the model to the evaluation of bulk retention capacities. The interface between the fluids is often unstable due to DNAPL properties. Analytical solutions stemming from the continuity equation do not explicitly consider the stability of the interface where displacement occurs (at the pore scale). Consequently, conventional models have not achieved DNAPL migration and source zone characterization at the pore scale. A different modeling technique similar to diffusion limited aggregation (DLA), developed by Witten and Sander (1983), was investigated for this purpose. A unique relationship between the model input parameter, the sticking probability, and the essential properties governing the DNAPL-water front displacement was developed. The stochastic aggregation model is the first DLA-based model successfully used to simulate a variety of laboratory experiments, both in homogeneous and heterogeneous porous media.

An evaluation of the model concludes that the model is well formulated for simulating two-dimensional DNAPL-water displacement for a variety of DNAPLs under the conditions of different inflow rates, different angles of inclination from the horizontal,

and varying heterogeneous media properties. The comparison of model simulations to laboratory experiments remains limited to visual inspection. This is the case for other models currently attempting to model DNAPL-water displacements.

The model was used to evaluate the bulk retention capacity for a variety of common DNAPLs. A bulk retention capacity can be determined for a specified bulk volume of soil, and the characteristic front displacement can be visualized using the stochastic aggregation model. The bulk retention capacity increases as the flow rate of the DNAPL increases, as the viscosity difference with water increases, and as the intrinsic permeability of the media decreases.

The use of this modeling technique in evaluating the problem of DNAPL source zone characterization is new. It is not yet developed to a stage that is ready for broad field-scale usage. There are many questions remaining to be answered before a broad application and extension of the model can occur. The following are recommendations for future research.

- The theoretical relationship between the capillary pressure gradient and the model's sticking probability should be established. This cannot be done until the mathematics behind incorporating a sticking probability into the model are known. If the theoretical link can be established, the model can be used to simulate three-dimensional displacement fronts.
- Scaling of the grid size should be investigated further by running very large simulations. The purpose of scaling the grid is to reduce the time necessary for simulations. It is reasonable to believe that the advancement of technology may take care

of this problem. There may no longer be a need for grid scaling if the time it takes to run large-sized grid simulations is improved.

- Grids of stochastically varying permeabilities should be generated and used with the model to produce simulations that are more representative of field conditions.

- An evaluation of the entry pressure should be incorporated into the model.

Incorporating an entry pressure determination into the model gives the model another piece of information on which to base decisions for the front movement. This entry pressure evaluation will lead to more accurate model simulations.

REFERENCES

- AATDF Technology Practices Manual for Surfactants and Cosolvents: Second Edition, 1997. Coauthors: Kueper, B. H., Pitts, M., Wyatt, K. Simpkin, T. and Sale, T. Advanced Applied Technology Demonstration Facility Program, Rice Univ. Energy and Environmental Systems Institute – MS316.
- Anderson, M. R., 1988. The dissolution and transport of dense non-aqueous phase liquids in saturated porous media. Ph.D. Dissertation, Oregon Graduate Center, Beaverton, OR, 266 pp.
- Baudet, C., Charlaix, E., Clement, E., Gyron, E., Hulin, F.-P., and Leroy, C., 1986. Scaling Concepts in porous media. Scaling Phenomena in Disordered Systems, edited by R. Dyam and A. Skjeltorp, NATO ASI Series B, Physics (133).
- Bedient, P. B., Rife, H. S. and Newell, C. J., 1994. Ground Water Contamination: Transport and Remediation. Prentice Hall PTR, Englewood Cliffs, NJ.
- Berkowitz, B. and Balberg, I., 1993. Percolation theory and its application of groundwater hydrology. Water Resour. Res., 29(4): 775-794.
- Birovljev, A., Furuberg, L., Feder, J., Jossang, T., Maloy, K. J. and Aharony, A., 1991. Gravity invasion percolation in two dimensions: experiment and simulation. Phys. Rev. Lett., 67(5): 584-587.
- Broadbent, S. R. and Hammersley, J. M., 1957. Percolation processes, crystals and mazes. Proc. Cambridge Philos. Soc., 53: 629-641.
- Brooks, R. H., and Corey, A. T., 1964. Hydraulic properties of porous media. Hydrol. Pap. 3, Civil Engineering Department, Colorado State University, Fort Collins.
- Catalan, L. J. J. and Dullien, F. A. L., 1995. Application of gravity drainage to the recovery of residual LNAPL in homogeneous and lensed sand packs. J. Contam. Hyd., 18: 279-306.
- Chatzis, I. and Dullien, F. A. L., 1985. The modeling of mercury porosimetry and the relative permeability of mercury in sandstones using percolation theory. Int. Chem. Eng., 25: 47-66.
- Chen, J.-D. and Wilkinson, D., 1985. Pore-scale viscous fingering in porous media. Phys. Rev. Lett., 55: 1892-1895.
- Corey, A. T., 1994. Mechanics of immiscible fluids in porous media. Water Resources Publications, Highlands Ranch, CO.

- Chuoque, R. L., Van Meurs, P., and van der Poel, C., 1959. The instability of slow immiscible, viscous liquid-liquid displacements in porous media. *Trans. A.I.M.E.*, 216: 188-194.
- Constantinides, G.N. and Payatakes, A. C., 1989. A three dimensional network model for consolidated porous media, *Basic studies. Chem. Eng. Commun.*, 81: 55-81.
- Daccord, G., Nittmann, J. and Stanley, H. E., 1986. Radial viscous fingers and diffusion-limited aggregation: fractal dimension and growth sites. *Phys. Rev. Lett.*, 56: 336-339.
- Dawson, H. E. and Roberts, P. V., 1997. Influence of viscous, gravitational, and capillary forces on DNAPL saturation. *Ground Water*, 35(2): 261-269.
- Dias, M. M. and Payatakes, A. C., 1986a. Network models for two-phase flow in porous media, 1, Immiscible microdisplacement of non-wetting fluids. *J. Fluid Mech.*, 164: 305-336.
- Dias, M. M. and Payatakes, A. C., 1986b. Network models for two-phase flow in porous media, 2, Motion of oil ganglia. *J. Fluid Mech.*, 164: 337-358.
- Dullien, F. A. L., 1992. *Porous Media: Fluid Transport and Pore Structure*. Academic, San Diego, CA.
- Fatt, I., 1956. The network model of porous media, I, Capillary pressure characteristics. *Trans. A.I.M.E. Pet. Dev.*, 207: 144-159.
- Feenstra, S. and Cherry, J. A., 1996. Diagnosis and assessment of DNAPL sites, in *Dense Chlorinated Solvents and other DNAPLs in Groundwater*, edited by J. F. Pankow and J. A. Cherry. Waterloo Press, Portland, OR, pp. 395-473.
- Fernandez, J. F., Rangel, R. and Rivero, J., 1991. Crossover Length from Invasion Percolation to Diffusion-Limited Aggregation in Porous Media. *Phys. Rev. Lett.*, 67: 2958-2961.
- Ferrand, L. A. and Celia, M. A., 1992. The effect of heterogeneity on the drainage capillary pressure saturation. *Water Resour. Res.*, 28(3), 859-870.
- Flury, M. and Fluhler, H., 1995. Modeling solute leaching in soils by diffusion-limited aggregation: Basic concepts and application to conservative solutes. *Water Resour. Res.*, 31(10): 2443-2452.
- Held, R. J. and Illangasekare, T. H., 1995a. Fingering of dense nonaqueous phase liquids in porous media 1. Experimental Investigation. *Water Resour. Res.*, 31(5): 1213-1222.

- Held, R. J. and Illangasekare, T. H., 1995b. Fingering of dense nonaqueous phase liquids in porous media 2. Analysis and Classification. *Water Resour. Res.*, 31(5): 1223-1231.
- Hilfer, R. and Øren, P. E., 1996. Dimensional analysis of pore scale and field scale immiscible displacement. *Transp. Porous Media*, 22: 53-72.
- Hill, S., 1952. Channelling in packed columns. *Chem. Eng. Sci.* 1: 247-253.
- Homsy, G. M., 1987. Viscous fingering in porous media. *Ann. Rev. Fluid Mech.* 19: 271-311.
- Illangasekare, T. H., Ewing, J. E. and Pytte, K. O., 1996. Process upscaling of nonaqueous phase liquid behavior in heterogeneous aquifers, *Non-Aqueous Phase Liquids (NAPLs) in Subsurface Environment: Assessment and Remediation*, ed. L. N. Reddi. ASCE, New York, pp. 25-45.
- Illangasekare, T. H., Ramsey, Jr., J. L., Jensen, K. H. and Butts, M. B., 1995. Experimental study of movement and distribution of dense organic contaminants in heterogeneous aquifers. *J. Contam. Hyd.*, 20: 1-25.
- Jerauld, G. R. and Salter, S. J., 1990. The effect of pore-structure on hysteresis in relative permeability and capillary pressure: Pore-level modeling. *Transp. Porous Media*, 5(2): 103-151.
- Johnson, R. L. and Kueper, B. H., 1996. Experimental Studies of the movement of chlorinated solvent compounds and other DNAPLs in the vadose, capillary and groundwater zones, in *Dense Chlorinated Solvents and other DNAPLs in Groundwater*, ed. J. F. Pankow and J. A. Cherry. Waterloo Press, Portland, OR, pp. 145-178.
- Jullien, R., Kolb, M. and Botet, R., 1984. Diffusion limited aggregation with directed and anisotropic diffusion. *J. Physique.*, 45: 395-399.
- Kadanoff, L. P., 1985. Simulating hydrodynamics: a pedestrian model. *J. Stat. Phys.*, 39(3/4): 267-283.
- Kaufman, J. H., Baker, C. K., Nazzari, A. I., Flickner, M. and Melroy, O. R., 1986. Statics and dynamics of the diffusion-limited polymerization of the conducting polymer polypyrrole. *Phys. Rev. Lett.*, 56: 1932-1935.
- Kiriakidis, D. G., Mitsoulis, E. and Neale, G. H., 1991. Linear displacement of a wetting fluid by an immiscible non-wetting fluid in a porous medium: a predictive algorithm. *Canadian J. Chem. Eng.*, 69: 557-563.

- Kueper, B. H. and Frind, E. O., 1988. An overview of immiscible fingering in porous media. *J. Contam. Hyd.*, 2: 95-110.
- Kueper, B. H., Abbot, W., and Farquhar, G., 1989. Experimental observations of multiphase flow in heterogeneous porous media. *Water Resour. Res.*, 23(4): 83-95.
- Kueper, B. H. and Frind, E. O., 1991a. Two-phase flow in heterogeneous porous media 1. Model development. *Water Resour. Res.*, 27(6): 1049-1057.
- Kueper, B. H. and Frind, E. O., 1991b. Two-phase flow in heterogeneous porous media 2. Model application. *Water Resour. Res.*, 27(6): 1059-1070.
- Kueper, B. H. and Gerhard, J. I., 1995. Variability of point source infiltration rates for two-phase flow in heterogeneous porous media. *Water Resour. Res.*, 31(12): 2971-2980.
- Kueper, B. H. and Frind, E. O., 1996. Numerical simulation of the migration of dense non-aqueous phase liquids (DNAPLs) in porous media, in *Dense Chlorinated Solvents and other DNAPLs in Groundwater*, ed. J. F. Pankow and J. A. Cherry. Waterloo Press, Portland, OR, pp. 129-144.
- Lake, L. W., 1989. *Enhanced Oil Recovery*. Prentice-Hall, Inc., Englewood Cliffs, NJ.
- Lenormand, R., Touboul, E. and Zarcone, C., 1988. Numerical models and experiments on immiscible displacements in porous media. *J. Fluid Mech.*, 189: 165-187.
- Lenormand, R., 1987. Statistical physics and immiscible displacements through porous media. *AIP Conference Proceedings 154, Physics and Chemistry of Porous Media II*, pp. 98-115.
- Li, Y., Laidlaw, W. G. and Wardlaw, N. C., 1986. Sensitivity of drainage and imbibition to pore structures as revealed by computer simulation of displacement process. *Adv. Colloid Interface Sci.*, 26: 1-68.
- Liang, S., 1986. Random-walk simulation of flow in Hele Shaw cells. *Phys. Rev. A*, 33(4): 2663-2674.
- Lowry, M. I. and Miller, C. T., 1995. Pore-scale modeling of nonwetting-phase residual in porous media. *Water Resour. Res.*, 31(3): 455-473.
- Mabey, W. R., Smith, J. H., Podoll, R. T., Johnson, H. L. Mill, T., Chou, T. W., Gates, J., Partridge, I. W., Jaber, H. and Vandenberg, D., 1982. Aquatic fate process data for organic priority pollutants. U. S. Environmental Protection Agency, Washington, D. C., Rep. No. 440/4-8-014.

- Maloy, K. J., Feder, J. and Jossang, T., 1985. Viscous fingering fractals in porous media. *Phys. Rev. Lett.*, 55: 2688-2691.
- Meakin, P., 1991. Fractal aggregates in geophysics. *Reviews of Geophysics*, 29(3): 317-354.
- Meakin, P., 1988. The growth of fractal aggregates and their fractal measures. *Phase Transitions and Critical Phenomena*, vol. 12, ed. C. Domb and J. L. Lebowitz, Academic, San Diego, CA, pp. 335-489.
- Meakin, P., 1986. Universality, nonuniversality, and the effects of anisotropy on diffusion-limited aggregation. *Phys. Rev. A*, 33(5): 3371-3382.
- Meakin, P. and Deutch, J. M., 1986. The formation of surfaces by diffusion limited annihilation. *J. Chem. Phys.*, 85(4): 2320-2325.
- Mercer, J. W. and Cohen, R. M., 1990. A review of immiscible fluids in the subsurface: Properties, models, characterization and remediation. *J. Contam. Hyd.*, 6: 107-163.
- Mercer, J. W., Adeel, Z., and Faust, C. R., 1996. A review of NAPL modeling approaches for remediation, *Non-Aqueous Phase Liquids (NAPLs) in Subsurface Environment: Assessment and Remediation*, ed. L. N. Reddi. ASCE, New York.
- Morrow, N. R. and Songkran, B., 1981. Effect of viscous and buoyancy forces on nonwetting phase trapping in porous media, in *Surface Phenomena in Enhanced Oil Recovery*, ed. D. O. Shah. Plenum Press, New York, pp. 387-411.
- Ng, K. M., Davis, H. T., and Scriven, L. E., 1978. Visualization of blob mechanics in flow through porous media. *Chem. Eng. Sci.*, 33: 1009-1017.
- Niemeyer, L., Pietronero, L. and Wiesmann, H. J., 1984. Fractal dimension of dielectric breakdown. *Phys. Rev. Lett.*, 52: 1033-1036.
- Nittmann, J., Daccord, G. and Stanley, H. E., 1985. Fractal growth of viscous fingers: quantitative characterization of a fluid instability phenomenon. *Nature*, 314: 141-144.
- Oreskes, N., Shrader-Frechette, K. and Belitz, K., 1994. Verification, validation, and confirmation of numerical models in the earth sciences. *Science*, 263: 641-646.
- Pankow, J. F., Feenstra, S., Cherry, J. A. and Ryan, M. C., 1996. Dense Chlorinated Solvents in Groundwater: Background and History of the Problem, in *Dense Chlorinated Solvents and other DNAPLs in Groundwater*, ed. J. F. Pankow and J. A. Cherry. Waterloo Press, Portland, OR, pp. 1-52.
- Pantazidou, M. and Sitar, N., 1993. Emplacement of nonaqueous liquids in the vadose zone. *Water Resour. Res.*, 29: 705-722.

- Paterson, L., 1984. Diffusion-limited aggregation and two-fluid displacements in porous media. *Phys. Rev. Lett.*, 52: 1621-1624.
- Poulsen, M. M. and Kueper, B. H., 1992. A field experiment to study the behavior of tetrachloroethylene in unsaturated porous media. *Environ. Sci. Technol.*, 26(5): 889-895.
- Saffman, P. G. and Taylor, G. I., 1958. The penetration of a fluid into a porous medium or Hele-Shaw cell containing a more viscous liquid. *Proc. Soc. London, Ser. A*, 245: 312-331.
- Sander, L. M., 1986. Fractal growth processes. *Nature*, 332(28): 789-793.
- Sander, L. M., 1984. Theory of Fractal Growth Processes. Kinetics of Aggregation and Gelation, ed. F. Family and D. P. Landau, Elsevier Science Publishers, B. V., pp. 13-17.
- Schroth, M. H., Istok, J. D., Ahearn, S. J. and Selker, J. S., 1995. Geometry and position of light nonaqueous-phase liquid lenses in water-wetted porous media. *J. Contam. Hyd.*, 19: 269-287.
- Schwille, F., 1988. Dense Chlorinated Solvents in Porous and Fractured Media. Lewis Publishers, Chelsea.
- Sherwood, J. D., 1987. Unstable fronts in a porous medium. *J. Comp. Phys.*, 68: 485-500.
- Soll, W. E. and Celia, M. A., 1993. A modified percolation approach to simulating 3-fluid capillary pressure saturation relationships. *Adv. Water Resour.*, 16(2): 107-126.
- Tsakiroglou, C. D. and Payatakes, A. C., 1990. A new simulator of mercury porosimetry for the characterization of porous materials. *J. Coll. Interface Sci.*, 137(2): 315-339.
- Wardlaw, N. C., Li, Y. and Forbes, D., 1987. Pore-throat size correlation from capillary pressure curves. *Transp. Porous Media*, 2: 597-614.
- Wiesmann, H. J. and Zeller, H. R., 1986. A fractal model of dielectric breakdown and prebreakdown in solid dielectrics. *J. Appl. Phys.*, 60: 1770-1773.
- Witten, T. A. and Sander, L. M., 1983. Diffusion-limited aggregation. *Physical Review B*, 27(9): 5686-5697.
- Wilkinson, D., 1984. Percolation model of immiscible displacement in the presence of buoyancy forces. *Physical Rev. A*, 30(1): 520-531.

Wilkinson, D. and Willemsen, J. F., 1983. Invasion percolation: A new form of percolation theory. *J. Phys. A Math. Gen.*, 16(14): 3365-3376.